



Research Article

Kinetics of UV degradation of hydrogen sulfide without oxidization by Homotopy Perturbation Method

Sreelatha DEVI^{1,*}, K. SARANYA¹, D. VIJAYABALAN², Jayanthi RAJENDRAN³,
Muthumari G⁴, Banu PRIYA V⁵

¹Department of Mathematics, Saveetha School of Engineering, SIMATS, Tamil Nadu, 600017, India

²Department of Mathematics, Vel tech high tech Dr. Rangarajan Dr. Sakunthala engineering college, Tamil Nadu, 600017, India

³Department of English, Associate Professor, Easwari Engineering college (SRM Group of Institution), Chennai, 516175, India

⁴Department of Mathematics, S.A. Engineering college, Tamil Nadu, 516175, India

⁵Department of Mathematics, R.M.K. College of Engineering and Technology, Chennai, 516175, India

ARTICLE INFO

Article history

Received: 28 May 2017

Accepted: 01 July 2025

Keywords:

H₂S; Homotopy Perturbation Method; Mathematical Modeling; Nonlinear Equations

ABSTRACT

The promotion of biogas energy has been constrained by the presence of H₂S. Classical H₂S photodegradation is typically carried out with oxygen present, but this is inappropriate for biogas desulfurization and must be prevented. Thus, the current study was to examine the UV degradation of H₂S without O₂ from a mathematical perspective. This paper was performing a theoretical investigation of UV degradation of H₂S without oxygen. First, the Homotopy perturbation approach was used to construct a theoretical computer model on H₂S photodegradation. This model included models for the distribution of gas flows, radiation kinetics in the photoreactor, mass balance, and degradation rate. Then, to verify the mathematical model, the effects of the initial H₂S concentration and gas retention duration on the photodegradation rate were examined. To validate the mathematical model, the effects of factors on the initiative H₂S mass and gas retention time toward the photo-degradation rate were investigated. The primary photodegradation products were identified as elemental S and H₂.

Cite this article as: Devi S, Saranya K, Vijayabalan D, Rajendran J, G M, B Priya V. Kinetics of UV degradation of hydrogen sulfide without oxidization by Homotopy Perturbation Method. J Ther Eng 2026;12(1):50–71.

INTRODUCTION

One of the persistent environmental and economic problems of the last century has been the capture and conversion of hydrogen sulfide (H₂S). Many important fuel gases, like natural gas, biogas, syngas, coke oven gas, landfill gas, and refinery gas, along with wastewater, have the very

unpleasant, smelly, and toxic chemical H₂S mixed in as a contaminant. For safety and economic reasons, this chemical must be removed from these streams. Equipment and pipeline corrosion results from H₂S's natural propensity to react with water to generate an acidic solution. Additionally, its presence causes catalyst poisoning and lowers the fuel

*Corresponding author.

*E-mail address: vijayabalantq@gmail.com

This paper was recommended for publication in revised form by
Editor-in-Chief Ahmet Selim Dalkilic



Published by Yildiz Technical University Press, İstanbul, Turkey

Yildiz Technical University. This is an open access article under the CC BY-NC license (<http://creativecommons.org/licenses/by-nc/4.0/>).

gases' heating value. Above all, as it burns, sulfur dioxide and other toxic sulfur oxides are released, which results in acid rain. Furthermore, H_2S is a toxic gas that is dangerous even at low quantities, as Table 1 illustrates. After extended exposure at roughly 5 ppm, it irritates the eyes and airways, and at 1000–2000 ppm, it instantly kills a person [1, 2]. Therefore, in order to improve the quality of life and the global atmospheric chemistry, H_2S emission needs to be reduced and controlled [3].

Therefore, purification is necessary to eliminate and/or convert H_2S (as well as other acid gases like CO_2) before many fuel gases can be used for energy generation or chemical manufacturing. The particular end use and the applicable municipal legislation determine the allowable level of H_2S in a gas stream. In the US and Denmark, for instance, pipeline gas must have an H_2S concentration of less than 4 parts per million [4], but reformer and fuel cell applications often need a content of less than 1 part per million [5, 6]. The two main categories of hydrogen sulfide capture techniques are physical chemical procedures and biological strategies. They can also be categorized as dry and wet desulfurization techniques. They can be further divided into cryogenic distillation, membrane separation, absorption, adsorption, microbiological techniques, advanced oxidation processes, etc. The current trends in each of these technologies, spanning the last five or ten years, are the main emphasis of this thorough assessment. Every one of them has benefits and drawbacks based on a variety of variables, which will be discussed here. However, because cryogenic distillation is expensive and has other practical problems that have hindered any significant technological advancement in H_2S removal over the last ten years [7], it is not covered in this work. However, whether the ultimate objective is to produce liquefied natural gas or to re-inject the liquefied acid gases into a geological reservoir, cryogenic separation, either as a stand-alone method or in conjunction with absorption, is probably the most cost-effective choice [8, 9, 10]. Through a two-step procedure, this study suggests an integrated and sustainable method for efficiently turning kitchen garbage into useful items. Using greenhouse solar drying is the first step in lowering the moisture content of kitchen waste. In the secondary process, kitchen waste is effectively broken down into biochar, biogas, and biooil using microwave pyrolysis. As renewable fuel sources, biogas and biooil are both viable. You can use biochar as a soil supplement. In [11] the environment is severely polluted as a result of rapid urbanisation and industrialisation, especially in water bodies that are tainted with dangerous germs and toxic dyes. Numerous studies have been conducted on zinc oxide (ZnO) nanoparticles because of their antibacterial and photocatalytic capabilities [12]. Synthetic dyes are widely used, particularly in the textile industry, which contributes to environmental contamination by introducing chemicals that are difficult to remove using conventional wastewater treatment methods. Complex aromatic structures provide these dyes stability and resilience, but they also produce harmful, frequently cancer-causing substances that endanger human health and aquatic habitats. This study suggests that

$\text{NiS-NiS}_2/\text{S-g-C}_3\text{N}_4$ is a strong and promising option for the reduction of aromatic nitro compounds [13]. Makes reference to the building many nations produce a lot of demolition and renovation waste (CDRW), and the building sector is a major driver of both infrastructure growth and socioeconomic advancement. The risks CDRWs pose to human health, safety, and the environment have prompted calls for action on a global scale. [14] A stronger turbulence velocity distribution, better mixture fraction values, and a lower soot formation distribution can be achieved by altering the bowl's shape [15]. Certain conditions must be met for the findings to be obtained. It was found that the pressure, temperature, and heat release of the combustion chamber had changed due to the modified bowl shape. [16] Hydrogen sulfide is an extremely hazardous, highly flammable, and extremely deadly gas that must be captured and removed from a number of important gaseous and liquid streams. Due to the persistent issue of H_2S trapping, a number of materials have been developed over time and used in a variety of technologies. Alkanolamines used as absorbents and metal oxides used as adsorbents are well-known examples. This research thoroughly examines the latest developments and state-of-the-art materials in this field. Biological methods, improved oxidation processes, metal organic frameworks, carbon-based materials, zeolites, ionic liquids, deep eutectic solvents, and polymeric membranes are a few examples. The state of the art is thoroughly examined in this review, which also provides a comprehensive technology map and identifies challenges and possibilities to guide future research. In the following publication, the technologies for H_2S removal and capture were described in detail. In the final study, H_2S removal and capture devices were thoroughly examined.

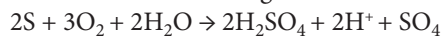
The paper has a significant contribution to developing [theoretical] models on the photodegradation of H_2S if UV radiation is in the absence of oxygen. Study derives analytical solutions for concentrations of H_2S and its degradation products using the HPM. For example, this model considers different factors including gas flow distribution, radiation kinetics, and mass balance to describe the photodegradation processes. H_2S techniques comprise biological, chemical, physical and combinatorial technologies. Several H_2S removal methods are carried out depending on physical, chemical, or biological principles. The potential of composite adsorbents is high, but their main challenge still revolves around selecting the optimum material combination and their synthesis. Some materials with chemisorption provide high capacity and breakthrough time, but they are often irreversible and would suffer from decreasing performance very quickly.

TECHNOLOGIES FOR H_2S CAPTURE / REMOVAL

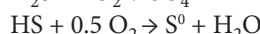
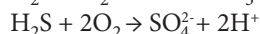
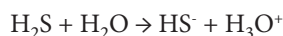
Biological Technologies

The foundation of biological approaches is the use of an oxidizing group of bacteria that thrives in environments where inorganic reduced sulfur compounds, like H_2S , are present. These gram-negative bacteria fall into

two categories: photoautotrophs and chemolithotrophs. They can use sulfur or sulfide as an electron source. Both domains share the following sulfur oxidation processes:



Some species, such as the ones listed above, biodegrade H_2S within the cell. However, extracellular oxidation of H_2S is also a feature of green sulfur bacteria, such as those of *Thiomicrospira frisia* and *Thiobacillus thioparus*. *Thiobacillus* species are commonly employed as chemotrophs for the biodegradation of H_2S due to their ability to thrive in various environmental settings. For instance, *Thiobacillus ferrooxidans* and *Thiobacillus thiooxidans* can thrive at low pH (<6). Being a thermophile, *Thermothrix azorensis* may survive at temperatures as high as 86°C. As an alkaliphile, *Thioalkalospira microaerophila* grows best at pH 10. The following illustrates the aerobic reactions for a colorless sulfur-oxidizing system. The amount of oxygen in this system affects the formation of elemental sulfur and the sulfate ion.



Some genera, including *Alcaligenes*, *Paracoccus*, *Pseudomonas*, *Xanthobacter*, and *Bacillus*, grow heterotrophically but have demonstrated the usage of reduced inorganic sulfur compounds in their metabolism, despite the fact that sulfur-oxidizing bacteria are typically autotrophic.

Absorption

The most popular method for purifying fuel gasses during the 20th century has been the absorption of acid gases into a liquid solvent. The strength of the solvent- H_2S interaction determines whether the absorption mechanism is classified as physical or chemical. Despite the strong interactions that characterize chemical absorption, stoichiometry limits it. There are almost no restrictions on solubility for physical absorption. At high pressures, physical absorption occurs, whereas chemical absorption often occurs at low pressures. Because of this, physical solvents like syngas cleaning—are superior to chemical solvents when the source gas has high partial pressures or concentrations of H_2S . Physical solvents can be renewed by air stripping, a straightforward pressure/temperature swing operation over one or more flash tanks, or by applying heat in a column, depending on the gas quality requirements. Chemical solvents are renewed by applying heat in a desorption column. It can be difficult to distinguish between physical and chemical absorbents because all solvents have physical interactions with solutes. Ionic liquids, deep eutectic solvents, alkanolamines, common physical solvents, and hybrid mixes are the five primary groups into which absorption techniques are divided for examination.

Adsorption

The process of surface-based adsorption transfers a molecule from a fluid bulk to the solid surface of the adsorbent. Under the topic of H_2S removal, we only discuss removal from a gas stream because this reaction is exothermic under dry conditions and does not require high temperatures. Recently, there has been a lot of interest in this dry desulfurization technology due to its affordability, adaptability, energy efficiency, and simplicity of usage. Adsorption is divided into two categories: physisorption and chemisorption (reactive adsorption), which are determined by the strength of the interaction between the adsorbent and adsorbate. Physisorption is dominated by van der Waals forces and/or electrostatic interactions, whereas chemisorption is dominated by covalent and/or hydrogen bonding interactions. Sometimes, regardless of the kind of underlying connection, the only way to distinguish between physisorption and chemisorption is based on contact intensity, particularly in experimental studies. In these situations, physisorption refers to weak contacts and chemisorption to strong ones. However, for molecules that are a little bit larger, physisorption can be rather robust. Apart from these interactions, selectivity in multi-component mixtures may also be impacted by the size and shape of molecules. High breakthrough capacity, chemical and thermal stability, structural regeneration, and selectivity towards target molecules (in this case, H_2S) are characteristics of desired adsorbent materials. Recently, a lot of research has been done on developing such economical and efficient adsorbents for the removal of H_2S , especially at low temperatures. In this regard, porous materials have emerged as intriguing options because of their large pore volume, large surface area, and range of potential chemical configurations.

Advanced Oxidation Processes

In order to speed up the breakdown of target molecules, Glaze initially classified advanced oxidation processes (AOPs) as those that produce and employ reactive species, primarily hydroxyl radicals ($HO\cdot$). $HO\cdot$ is a well-known highly oxidant species. Its redox potential is 2.8 V, which is lower than fluorine's (3.03 V) and greater than other known oxidants including ozone, hydroperoxyl, chlorine, permanganate, persulfate anion, hydrogen peroxide, and sulphate radicals. AOPs are now widely used to remove a wide range of contaminants from various industrial matrices, including contaminated air and streams. The many types of AOPs include Fenton and electro-Fenton processes, systems mediated by ozone (O_3) and hydrogen peroxide (H_2O_2), photocatalysis, photoirradiated processes, and plasma-based processes. All of these processes result in the production of $HO\cdot$, which breaks down the target molecules. According to the literature, there are several important ways in which AOPs are better than rival technologies. These include excellent yields and mineralization, the ability to operate at ambient conditions, long-term

performance stability, minimal mass transfer restrictions, a small footprint, little to no sludge formation, and high efficiency in incredibly quick reaction times. Among the disadvantages that researchers have identified are the toxicity of residual H_2O_2 in the effluent, the need for UV light to activate catalysts, the expense of the photo-reactor, and the decrease in photo-mediated process efficiency when suspended solids or less soluble salts are present (more likely for the H_2S oxidation process). However, the disadvantages of the conventional AOPs can be lessened by employing the synergy between the different strategies and combination AOPs, such as photocatalytic / H_2O_2 reactors, or more modern systems, such as UV-v is / catalyst. AOPs have been used in a few recent studies to oxidize gaseous and aqueous H_2S .

Electrochemical Processes

Electrochemical technology have been utilized for environmental cleaning for the last three decades. But around half a century ago, it was discovered that an electrochemical unit might be used to extract and /or oxidize hydrogen sulfide from aqueous solutions. In an electrochemical unit, an electron flow produced by external power sources triggers a series of oxidation and reduction reactions. It may be more cost-effective to employ chemical-less electrical oxidation than chemical-intensive methods, which require the dosing, transportation, and storage of potentially dangerous materials. The performance of the cell may also be readily regulated by varying operational parameters like voltage and current, and there is no limit on electron flow, unlike some technologies like photocatalytic reactors. Sometimes the primary concern in outdoor applications is the energy cost of an electrochemical cell. When renewable energy sources are employed, this method can be a flexible and sustainable technology that can be applied to a range of concentrated waste streams with excellent operating and energy efficiency. It can also be readily integrated with remote applications.

Membranes

Since membrane technology only started to be applied in industry in the latter half of the 20th century, it is relatively new in comparison to more established gas separation methods like adsorption and absorption. Even though membrane research dates back to the 19th century, Loeb and Sourirajan's invention of the first cellulose-acetate-based reverse osmosis membrane for water desalination in early 1962 marked the development of the first synthetic membranes on an industrial scale. It was not until the 1980s that membrane businesses made their way into the gas processing industry. Since then, one of the most important methods for gas separation has been polymeric membrane technology, which has shown remarkable performance and efficiency in gas transport. Membranes can optimize gas separation by (a) reducing equipment size and capital costs, (b) improving process safety and operating

simplicity, (c) doing away with complex control systems, and (d) requiring less energy, particularly when pressured gas is already available. In general, inorganic membranes are only utilized in systems when the direct use of polymeric membranes is prohibited by high temperatures and other working conditions due to their higher cost and manufacturing challenges. Consequently, polymeric membranes are currently the most often used materials for gas separation and/or natural gas sweetening. In order to focus on polymeric membranes that are used and evaluated for H_2S separation in natural gas purification, inorganic membranes will not be considered in this research. Over the past decade or so, research in this field has concentrated on attaining process stability and developing more robust and long-lasting materials in an attempt to enhance gas separation performance. H_2S studies are considerably more limited because of the toxicity of the gas and the extremely high purity requirements (down to ppm) that membranes alone can hardly accomplish. Membranes are usually researched for CO_2 collection and purification when dealing with acid gas removal. Since polymeric membranes have a high chemical endurance and have been shown to function well in harsh environments, they can be a highly useful pretreatment to increase the effectiveness of other technologies for purifying streams with high H_2S concentrations. The bulk of membrane applications are really focused on purifying natural gas, which contains 10–20% or even higher levels of hydrogen sulfide.

Anaerobic digestion, which is thought to be one of the most important methods for generating clean biogas fuel from biomass and generating renewable energy [17], also produces hydrogen sulphide [H_2S], which contains 0.3% to 0.4% of CH_4 and CO_2 [18]. Along with the potential for significant equipment, instrument, and pipeline damage, H_2S is an unpleasant acid gas. In addition, H_2S pollutes the environment and damages human health. As soon as the biogas is used as energy (for burning, electricity generation, etc.), the H_2S in it will be converted to SO_2 , which might significantly aggravate air pollution [19]. Therefore, H_2S must be removed from biogas using effective techniques because its presence delays the promotion of biogas energy. Chemical, physical, biological, and combinatorial technologies are all included in H_2S approaches. Because it can recycle hydrogen energy and effectively manage the H_2S pollution produced during the processing of coal, oil, gas, and minerals, the direct breakdown of H_2S to produce sulphur and hydrogen has been the focus of research by both domestic and foreign researchers. The main H_2S degradation processes that produce hydrogen and sulphur are thermal [20, 21], electrochemical [22], photocatalytic [23–25], and plasma degradation [26, 27]. The most promising method now in use is photocatalytic H_2S degradation due to its high treatment efficacy and response mobility [28]. Important new information on the efficacy of different wavelengths for this purpose has been obtained from experiments into the wavelength dependency and photosensitiser effects in UV-LED

photodegradation of iohexol [29]. The efficient photocatalytic degradation of 24 imidazolium ionic liquids is studied in an N-ZnO/simulated solar irradiation system, providing a comprehensive technique for this degradation process [30]. Throughout the entire study, the homotopy perturbation method was employed. The Homotopy Perturbation Method is a useful method for analyzing the kinetics of UV degradation of H_2S without O_2 in order to manage nonlinearities, give efficient approximations, and obtain a deeper comprehension of the reaction dynamics. Greater planning for environmental management will result from a greater understanding of the deteriorating process.

The photodegradation of H_2S is carefully examined in this work utilizing a vacuum ultraviolet (VUV) lamp in the absence of oxygen. The initial step of the study is to model the photodegradation process using MATLAB software. It investigates the effects of altering the starting H_2S concentration and exposure time on degrading results, contrasting these actual findings with the model's predictions. The investigation also explores the mechanisms and reaction kinetics of H_2S degradation in the absence of oxygen. It is anticipated that the results of this study will make a substantial contribution to the effective removal of H_2S in anaerobic settings, improving the sustainability and feasibility of biogas as a renewable energy source.

MATERIALS AND METHODS

Tests and The Reactor

Figure 1 shows the H_2S photodegradation reaction or process used in this investigation schematically. The reactor's cylindrical shape was chosen to prevent photodegradation dead space and possible uneven gas distribution inside the reactor. Silica gel, which is resistant to corrosion and high temperatures, sealed the cylindrical VUV lamp and reactor. The lamp was set above the reactor. An external

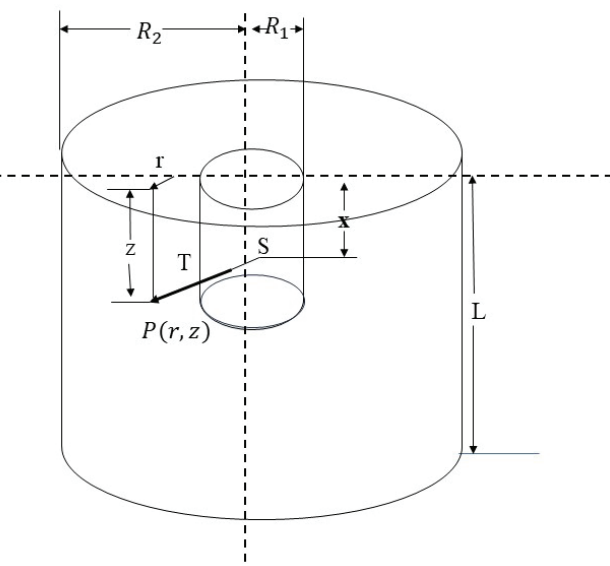


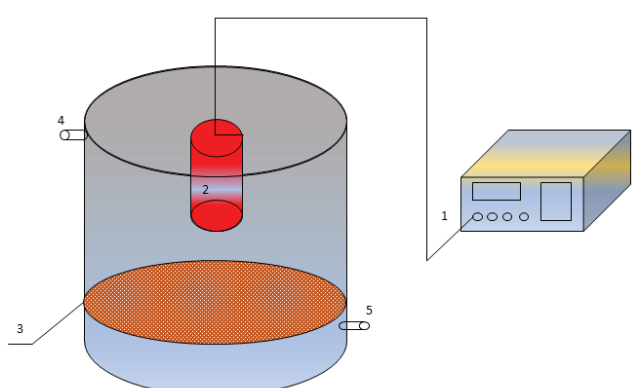
Figure 2. Cylindrical light source and Cylindrical photoreactor.

circuit was used to connect the VUV lamp to a high-frequency generator. At the gas entrance, a porous plate-like gas distribution device was attached, allowing the incoming gas to flow upward uniformly. The reactor's gas exit was situated atop it. The reactor's gas input and outlet were positioned on opposite sides to prevent short flow. The reactor's body was constructed of SUS 304 stainless steel to protect it from high-frequency electromagnetic radiation and to stop H_2S -induced corrosion. The reactor measured 14 cm in height and 15 cm in diameter. The reactor's overall capacity was 2.5 L, but with the addition of a cylindrical UV lamp that was 5.8 cm in height and 4 cm in diameter, the effective volume was 2.0 L.

The cylindrical photoreactor with a cylindrical light source for radiation field modelling is diagrammatically sketched in Figure 2, where $I(r, z)$ is the light intensity at point $P(r, z)$ within the reactor, $S_{(L\lambda)}$ is the UV intensity at wavelength λ , and r and z are the vertical and horizontal distances of the random particles from the UV lamp's centre, respectively. The UV lamp's length is L . At the wavelength of λ , the medium's absorption coefficient in the reactor is denoted by $\mu\lambda$. The cylindrical reactor's radii are denoted by R_2 and the cylindrical UV lamps by R_1 .

Experimental Methods

The reactor was first dried, and Ar was flushed into it at a rate of 10 L / min for an hour in order to remove any remaining O_2 and H_2O from the pipeline. This was done to examine the efficiency of H_2S degradation using only the high-frequency electrodeless VUV lamp without the addition of O_3 , OH , and photocatalyst. To eliminate the impact of O_3 and OH on H_2S degradation, Ar gas was continually flushed during the experiment.



1. Generator with high frequency, 2. Distribution of gas equipment, 3. Electrodeless VUV lamp, 4. Gas outlet, 5. Gas inlet.

Figure 1. H_2S photo degradation reactor.

The experimental method was intended to maximize the reliability and reproducibility of the results. Natural gas is passed through a sealed cylindrical quartz photoreactor where the interior is flushed with argon gas at a solvent flow rate of 10 L/min to effectuate elimination of oxygen and water vapor. H_2S degradation was tested spectrophotometrically using the methylene blue method at 660 nm, assuring quantitative accuracy. The light intensity inside the reactor was theoretically computed and measured using a calibrated UV radiometer. The experiments were performed at constant ambient environmental conditions to prevent any variation. For any run, the initial concentration of H_2S was held steady. Every test was carried out thrice, and the reported data represent the averages. Errors were estimated during measurement and incorporated as a factor in the kinetic evaluation to compensate for the data dispersion so as to arrive at a more conclusive result.

Analytical Methods

H_2S concentration was determined with methylene blue spectrophotometry under a wavelength of 660 nm.

In Figure 3, the cylindrical VUV lamp at the centre of the photoreactor, which has a diameter of 15 cm and a height of 14 cm, is used to replicate the light intensity in three dimensions. As scaled on the figure coordinate axis, the VUV lamp occupied the white area, measuring 4 cm in diameter and 5.8 cm in height. Figure 3 shows that when one moves farther away from the centre of the light source, the intensity of the light gradually decreases. The UV_{254} intensity was measured using a UV radiation meter 5 to 35 cm from the cylindrical lamp's wick to confirm the outcome of the light intensity distribution model in the reactor. The UV light radiation field model was used to compute the light intensity at the same location, and the model's output was confirmed by comparing it with the measured value.

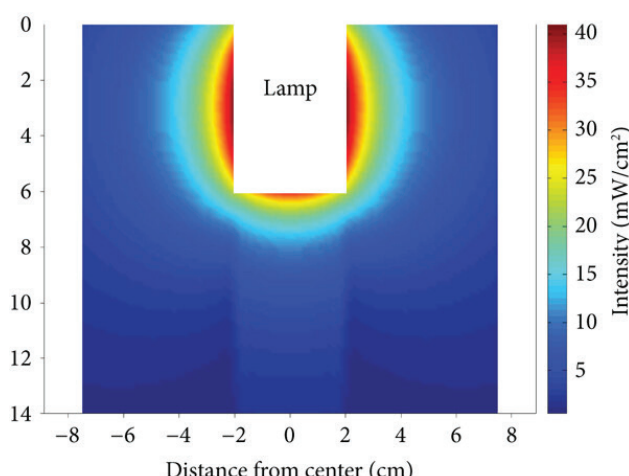
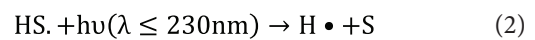
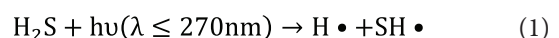


Figure 3. The distribution of light intensity within the photoreactor.

The methylene blue spectrophotometric technique was used to quantify the H_2S degradation, the residual H_2S in the gas phase being absorbed into a zinc acetate solution and reacting with N,N-dimethyl-p-phenylenediamine and ferric chloride to form methylene blue. The absorbance of this solution was then measured at 660 nm in a UV-Vis spectrophotometer. Calibration with standard H_2S solutions ensured the proper quantification of absorbed gases, and linearity of the calibration curve was verified within the specified concentration range under investigation. Each experiment was duplicated thrice to ensure results reproducibility and averages reported. The standard deviation among replicates was below $\pm 5\%$, attesting to consistent performance. Measurement uncertainty results predominantly from spectrophotometric readings and from incongruity in gas concentrations, which were minimized by means of right instrument calibration complemented by controlled flow rates on gas introduction.

Mathematical Formulation of The Problem

A thorough study of the direct photodegradation of hydrogen sulfide (H_2S) caused by photons in the incoming ultraviolet (UV) band was carried out by Wilson et al. [31]. Their examination showed that photons with wavelengths shorter than 270 nm could start the breakdown process, causing H_2S to produce hydroxyl radicals ($\text{H}\cdot$) and sulfhydryl radicals ($\text{SH}\cdot$). Moreover, further photon exposure, particularly with wavelengths less than 230 nm, facilitated the transformation of $\text{SH}\cdot$ into $\text{H}\cdot$ and sulfur radicals ($\text{S}\cdot$), as corroborated by experimental evidence (1) and (2). These reactions illustrate the complex interplay between H_2S and UV radiation, highlighting the formation of reactive intermediates such as radicals and their subsequent reactions with oxygen and other species present in the environment. A substantial amount of study has been done previously on the creation and improvement of photocatalytic materials for a range of uses. Using a flower-shaped nanophotocatalyst, a novel model is created for the kinetics and mass transfer in the sun-light-driven photodegradation of malachite green. The process is optimized by applying both machine learning and deep learning techniques [32]. Through high-efficiency photogenerated carrier transport, Wang et al. investigated a novel 2D/2D S-scheme heterojunction photocatalyst for peroxymonosulfate activation, which permits rapid degradation of ciprofloxacin [33]. Further elucidation of these reaction pathways is crucial for understanding the fate and impact of H_2S photodegradation in various environmental settings.



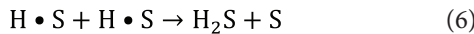
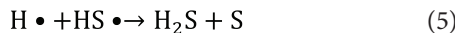


Table 1 summarizes the rate constants for the aforementioned reactions, which may be obtained by consulting the National Institute of Standards and Technology's (NIST) chemical dynamics database and relevant literature. The molar absorption coefficients for wavelengths of 185 nm and 254 nm can be determined by converting the absorptivity values given in Table 1, and a photon takes part in reactions (1) and (2). The degradation rate equation of the different intermediates during hydrogen sulfide photodegradation in the absence of O_2 may be established based on (1), (2), (3), (4), (5), and (6). Let $k_{obs} = 2030\phi_i\epsilon b$ ((4)), noting k_{obs1} , k_{obs2} , k_3 , k_4 , k_5 , and k_6 as the rate constants for (1), (2), (3), (4), (5), and (6), as the photon is shown in (1) and (2). Each component's reaction rate equations can be written as follows:

$$\left(\frac{d[H_2S]}{dt}\right) = -k_{obs1}[H_2S] - k_3[H_2S][H \cdot] + k_6[SH \cdot] \quad (7)$$

$$\left(\frac{d[H \cdot]}{dt}\right) = k_{obs1}[H_2S] + k_{obs2}[SH \cdot] - k_3[H_2S][H \cdot] + k_4[H \cdot]^2 - k_5[SH \cdot][H \cdot] \quad (8)$$

$$\left(\frac{d[SH \cdot]}{dt}\right) = k_{obs1}[H_2S] + k_{obs2}[SH \cdot] - k_5[SH \cdot][H \cdot] - k_6[SH \cdot]^2 \quad (9)$$

following circumstances: Initially, the H_2S concentration was fixed at 12 mg/m³, and the carrier gas was Ar. MATLAB software was used to determine the concentration evolution of H_2S , $H \cdot$, $SH \cdot$, H_2 , and S at a distance of 2 cm from the UV light. The logarithmic scale in Figure 4 illustrates this process. It was discovered that the primary end products of H_2S photodegradation were H_2 and S , and that their concentrations were quite near to one another, which was consistent with the photodegradation reaction's stoichiometric constants. Furthermore, compared to H_2 and S , the simulated concentrations of $H \cdot$ and $SH \cdot$ radicals were very low, around two orders of magnitude lower. In the end, we attempted to use the steady-state approximation for radicals to construct the analytical equation that links the rate of H_2S consumption with its concentration and light intensity.

The initial conditions given below

$$\begin{aligned} t = 0, \quad H_2S &= H_2S_{ini} \\ t = 0, \quad H \cdot &= H_{ini} \\ t = 0, \quad SH \cdot &= SH_{ini} \\ t = 0, \quad H_2 &= H_2_{ini} \\ t = 0, \quad S &= S_{ini} \end{aligned} \quad (12)$$

The boundary conditions are

$$\begin{aligned} t = 0, \quad H_2S &= 0 \\ t = 0, \quad H \cdot &= 0 \\ t = 0, \quad SH \cdot &= 0 \\ t = 0, \quad H_2 &= 0 \\ t = 0, \quad S &= 0 \end{aligned} \quad (13)$$

Reaction	Quantum efficiency	Light absorptivity at 185nm	Light absorptivity at 254nm	Rate constant	Reaction order	References
$H_2S + h\nu(\lambda \leq 270\text{nm}) \rightarrow H \cdot + SH \cdot$	1	1004.66	1.96	/	/	[48]
$HS \cdot + h\nu(\lambda \leq 230\text{nm}) \rightarrow H \cdot + S$	1	20.5	0	/	/	[48]
$H \cdot + H_2S \rightarrow H_2 + SH \cdot$	/	/	/	2.498E+10	2	[49]
$H \cdot + H \cdot \rightarrow H_2$	/	/	/	4.786E+08	2	[50]
$H \cdot + HS \cdot \rightarrow H_2S + S$	/	/	/	8.0E+09	2	[51]
$H \cdot S + H \cdot S \rightarrow H_2S + S$	/	/	/	8.368E+9	2	[52]

$$\left(\frac{d[H \cdot]}{dt}\right) = k_3[H_2S][H \cdot] + k_4[H \cdot]^2 + k_5[SH \cdot][H \cdot] \quad (10)$$

$$\left(\frac{d[S]}{dt}\right) = k_{obs2}[SH \cdot] - k_5[SH \cdot][H \cdot] - k_6[SH \cdot]^2 \quad (11)$$

The UV-photodegrading reactor model was then modified to incorporate the reaction rate equations for H_2S , $H \cdot$, $SH \cdot$, H_2 , and S (from (7), (8), (9), (10), and (11) and simulate the H_2S photodegradation effect without O_2 under the

APPROXIMATE ANALYTICAL REPRESENTATION FOR THE CONCENTRATION OF H_2S PHOTODEGRADATION AND THE CORRESPONDING REACTION RATE EQUATIONS FOR H_2S , H , $SH \cdot$, H_2 AND S USING HPM

Recently, in engineering and physics disciplines, so many researchers used the Homotopy perturbation method and fractional calculus to solve a variety of nonlinear issues [34-38, 42-44]. This approach combines standard perturbation

scheme with topology. Ji Huan, He utilized the Homotopy perturbation method to solve the light hill equations [39] the Duffing [40] and the Blasius [41]. This method is distinct in its efficiency, precision, and applicability. The Homotopy perturbation method (HPM) has demonstrated its versatility and effectiveness across various scientific domains, particularly in addressing complex nonlinear problems. HPM is applied in the context of kinetic modeling to study the degradation of total organic carbon in dairy wastewater, showcasing its ability to model and solve intricate biochemical reaction systems in environmental technology. This application highlighted HPM's capability to simplify and accurately predict the degradation kinetics of organic compound [45]. A constrained Homotopy method is utilized for parameter estimation in nonlinear diffusion problems. Their research underscored HPM's strengths in managing the constraints and complexities inherent in such equations, leading to more precise

parameter estimations. This approach has proven beneficial in fields where accurate modeling of diffusion processes is crucial, such as in material science and thermal analysis [46]. An approach to regularization Homotopy for limited parameter inversion of partial differential equations is presented. This study highlighted the robustness of HPM in stabilizing the inversion process, making it a reliable tool for tackling ill-posed problems. By incorporating regularization techniques, they enhanced the reliability and stability of the solutions, which is particularly valuable in entropy-based studies and other applications requiring precise parameter inversion [47]. In order to find an asymptotic result, the Homotopy perturbation approach uses the surrounding parameter p as a tiny parameter and requires extremely little duplication. Analytical formulas for the concentrations of H_2S , $H\bullet$, $SH\bullet$, H_2 , and S are derived from these equations using the Homotopy perturbation method with HPM, yielding the following outcomes:

$$[H_2S]t = c_1 e^{-at} + \frac{1}{c_4} \left((L_1 - L_4 t) e^{-at} - L_2 e^{-at-bt} + L_3 e^{-2at} + c_{18} e^{-2bt} \right) \quad (14)$$

$$\begin{aligned} [H\bullet]t &= c_3 e^{-at} + e^{-bt} - c_2 \\ &+ \frac{a}{4} \left(L_1 \left(\frac{e^{-at}}{-a} \right) - L_4 \left(t \frac{e^{-at}}{-a} - \frac{e^{-at}}{a^2} \right) \right. \\ &\quad \left. - L_2 \left(\frac{e^{-(a+b)t}}{-(a+b)} \right) + L_3 \left(\frac{e^{-2at}}{-2a} \right) + c_{18} \left(\frac{e^{-2bt}}{-2b} \right) \right) \\ &+ \frac{b}{p_{98}} \left(A_1 \left(\frac{e^{-2bt}}{-2b} \right) - A_2 \left(\frac{e^{-bt}}{-b} \right) + (p_{43} - p_{71} - p_{91}) \left(t \frac{e^{-bt}}{-b} - \frac{e^{-bt}}{b^2} \right) \right. \\ &\quad \left. + (A_3 + A_6) \left(\frac{e^{-(a+b)t}}{-(a+b)} \right) - A_4 \left(\frac{e^{-at}}{-a} \right) + (p_{16} - p_{44} - p_{72}) \left(t \frac{e^{-at}}{-a} - \frac{e^{-at}}{a^2} \right) \right) \end{aligned} \quad (15)$$

$$\begin{aligned} &- A_4 \left(\frac{e^{-at}}{-a} \right) + (p_{16} - p_{44} - p_{72}) \left(t \frac{e^{-at}}{-a} - \frac{e^{-at}}{a^2} \right) \\ &- k_3 \left(c_1 c_3 \left(\frac{e^{-2at}}{2a} \right) + c_1 \left(\frac{e^{-(a+b)t}}{-(a+b)} \right) - c_1 c_2 \left(\frac{e^{-at}}{-a} \right) \right) \\ &+ k_4 \left(\left((c_3)^2 \frac{e^{-2at}}{-2a} \right) + 2c_3 \left(\frac{e^{-(a+b)t}}{-(a+b)} \right) - 2c_2 c_3 \left(\frac{e^{-at}}{-a} \right) + 2c_2 \left(\frac{e^{-bt}}{-b} \right) - 2c_2 \left(\frac{e^{-bt}}{-2b} \right) + t(c_2)^2 \right) \\ &+ k_5 \left(\left(A \frac{e^{-(a+b)t}}{(a+b)} \right) + A c_3 \left(\frac{e^{-2at}}{2a} \right) - A c_2 \left(\frac{e^{-at}}{-a} \right) + B c_3 \left(\frac{e^{-(a+b)t}}{(a+b)t} \right) - B c_2 \left(\frac{e^{-bt}}{-b} \right) + B \left(\frac{e^{-2bt}}{-2b} \right) \right) \end{aligned} \quad (16)$$

$$[SH\bullet]t = A e^{-at} + B e^{-bt} + \frac{e^{-3at-3bt}}{p_{98}} \left(\begin{array}{l} A_1 e^{3at} + e^{3at+bt} (A_2 + p_{43}t - p_{71}t - p_{91}t) \\ + (A_3 + A_6) e^{(2a+b)t} + e^{(2a+2b)t} (A_4 + p_{16}t - p_{44}t - p_{72}t) \\ + A_5 e^{(2a+2b)t} \end{array} \right) \quad (16)$$

Table 1. Shows the plot of influence concentration profile and time t computed with Eq. (16) in Figure 7

t	Values of k_{obs1}				Values of k_{obs2}				Values of k_5				Values of k_6			
	0.4	0.5	1	2	0.05	0.09	0.13	0.23	0.2	1.8	2.6	3.8	0.02	0.4	0.16	0.25
0	0.0018	0.0004	0.0018	0.0019	0.0019	0.0019	0.0017	0.0008	0.0016	0.0016	0.0016	0.0016	0.0390	0.0083	0.0277	0.0204
0.4	0.0291	0.0457	0.0943	0.1589	0.2235	0.1087	0.0645	0.0208	0.0551	0.0895	0.1067	0.1325	0.0680	0.0193	0.0501	0.0385
.8	0.0523	0.0792	0.1508	0.2214	0.3659	0.1746	0.1013	0.0295	0.0860	0.1453	0.1749	0.2193	0.1083	0.0361	0.0817	0.0646
1.2	0.0694	0.1035	0.1839	0.2428	0.4559	0.2140	0.1217	0.032	0.1032	0.183	0.2229	0.2828	0.1331	0.0488	0.1020	0.0821
.6	0.0817	0.1207	0.2021	0.2466	0.5114	0.2362	0.1318	.0315	0.1120	0.2106	0.2599	0.3338	0.1489	0.0594	0.1159	0.0947
2	0.0902	0.1324	0.2108	0.2429	0.5441	0.2473	0.1355	0.0295	0.1157	0.2324	0.2907	0.3782	0.1595	0.0689	0.1261	0.1046

$$[H_2]t = H_2 \text{ini} + k_3 \left(c_1 c_3 \left(\frac{e_1^{-2at}}{2a} \right) + c_1 \left(\frac{e_1^{-(a+b)t}}{-(a+b)} \right) - c_1 c_2 \left(\frac{e_1^{-at}}{-a} \right) \right) + k_4 \left(\left((c_3)^2 \frac{e_1^{-2at}}{-2a} \right) + 2c_3 \left(\frac{e_1^{-(a+b)t}}{-(a+b)} \right) - 2c_2 c_3 \left(\frac{e_1^{-at}}{-a} \right) + 2c_2 \left(\frac{e_1^{-bt}}{-b} \right) - 2c_2 \left(\frac{e_1^{-bt}}{-2b} \right) + t(c_2)^2 \right) + k_5 \left(\left(A \frac{e_1^{-(a+b)t}}{(a+b)} \right) + A c_3 \left(\frac{e_1^{-2at}}{2a} \right) - A c_2 \left(\frac{e_1^{-at}}{-a} \right) + B c_3 \left(\frac{e_1^{-(a+b)t}}{(a+b)t} \right) - B c_2 \left(\frac{e_1^{-bt}}{-b} \right) + B \left(\frac{e_1^{-2bt}}{-2b} \right) \right) \quad (17)$$

Table 2. Show the plot of influence concentration profile and time t computed with Eq. (17) in Figure 8

t	Values of k_3				Values of k_4				Values of k_5			
	0.01	0.021	0.033	0.0005	0.5	1	1.5	2	0.1	0.6	1.1	1.3
0	0.1	0.1	0.0999	0.0999	0.1	0.1	0.0999	0.0999	0.0999	0.0999	0.1	0.1
0.2	0.0998	0.0994	0.0989	0.1002	0.0972	0.0987	0.1002	0.1016	0.0972	0.0971	0.097	0.097
0.4	0.1	0.0991	0.0982	0.1007	0.0964	0.1003	0.1043	0.1083	0.0963	0.0958	0.0954	0.0952
0.6	0.1004	0.0993	0.0981	0.1014	0.0973	0.105	0.1127	0.1204	0.0972	0.096	0.0948	0.0943
0.8	0.1012	0.0998	0.0983	0.1023	0.1001	0.1128	0.1255	0.1382	0.0998	0.0975	0.0953	0.0945
1	0.1022	0.1006	0.0989	0.1035	0.1046	0.1237	0.1427	0.1617	0.1041	0.1005	0.0969	0.0955

$$[S]t = b \left(A \frac{e_1^{-at}}{-a} + B \frac{e_1^{-bt}}{-b} \right) + S_{\text{ini}} + b \left(\frac{A}{a} + \frac{B}{b} \right) + \frac{b}{p_{98}} \left(A_1 \left(\frac{e_1^{-2bt}}{-2b} \right) - A_2 \left(\frac{e_1^{-bt}}{-b} \right) + (p_{43} - p_{71} - p_{91}) \left(\left(t \frac{e_1^{-bt}}{-b} \right) - \left(\frac{e_1^{-bt}}{b^2} \right) \right) \right) + (A_3 + A_6) \left(\frac{e_1^{-(a+b)t}}{-(a+b)} \right) - A_4 \left(\frac{e_1^{-at}}{-a} \right) + (p_{16} - p_{44} - p_{72}) \left(t \frac{e_1^{-at}}{-a} - \frac{e_1^{-at}}{a^2} \right) + k_5 \left(A c_3 \left(\frac{e_1^{-2at}}{2a} \right) + B c_3 \left(\frac{e_1^{-(a+b)t}}{(a+b)t} \right) + A \left(\frac{e_1^{-(a+b)t}}{(a+b)} \right) + B \left(\frac{e_1^{-2bt}}{-2b} \right) - A c_2 \left(\frac{e_1^{-at}}{-a} \right) - B c_2 \left(\frac{e_1^{-bt}}{b} \right) \right) + k_6 \left(A^2 \left(\frac{e_1^{-2at}}{-2a} \right) + 2AB \left(\frac{e_1^{-(a+b)t}}{(a+b)} \right) + B^2 \left(\frac{e_1^{-2bt}}{-2b} \right) \right) \quad (18)$$

Table 3. Shows plot of influence concentration profile and time t computed with Eq. (18) in Figure 9

t	Values of k_3				Values of k_4				Values of k_5			
	0.1	0.09	0.13	0.2	0.5	0.6	0.7	0.8	9	12	16	19
1	8.4596	9.2418	6.9606	5.226	1.5647	1.6376	1.7106	1.7836	4.7035	3.4366	1.7475	0.4806
2	8.2740	9.0277	6.7176	4.9424	1.5536	1.6244	1.6951	1.7658	4.9004	3.773	2.2707	1.1437
3.5	7.7755	8.5454	6.1784	4.3423	1.5287	1.5944	1.6602	1.7260	5.1629	4.2901	3.1264	2.2536
5	7.1948	7.9785	5.5687	3.7050	1.4997	1.5596	1.6196	1.6795	5.2361	4.5818	3.7093	3.0550
6.5	6.5877	7.3811	4.9395	2.9717	1.4693	1.5232	1.5771	1.6309	5.1296	4.6425	3.9930	3.5059
8	5.9311	6.7463	4.1752	1.2797	1.4365	1.4838	1.5311	1.5784	4.8360	4.4701	3.9823	3.6164

By contrasting analytical predictions with experimental findings from earlier research, Figure 4 investigates the impact of different concentrations on the

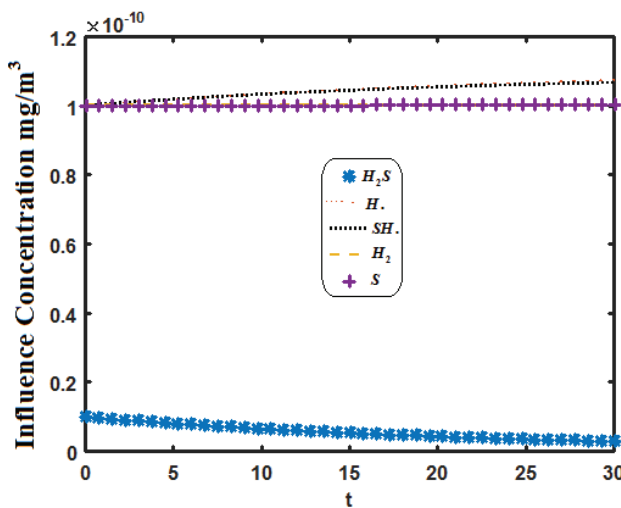


Figure 4. Represents influence concentration for different values and compared experimental results.

degradation process [28]. This comparison demonstrates the analytical model's relevance in practical situations and verifies it.

Figure 5 explores the connection between the initial concentration of H_2S and the gas's retention time. It implies that while the observed rate constant ($k_{\text{obs}1}$) falls, the concentration of H_2S increases as the constants k_3 and k_6 grow, indicating higher reaction rates. This may suggest that saturation effects brought on by increased H_2S concentrations could lower the overall degradation efficiency.

Reaction Dynamics and Radicals

Figure 6 illustrates how $k_{\text{obs}1}$, k_1 , and k_5 drop as the simulated concentration of hydrogen radicals ($\text{H}\cdot$) rises. This suggests that some chemical routes may become less advantageous as the concentration of $\text{H}\cdot$ increases, changing the kinetics of the degradation process. The concentration of thiol radicals ($\text{SH}\cdot$) rises in Figure 7, as $k_{\text{obs}1}$ and k_5 rise and $k_{\text{obs}2}$ and k_6 fall. This implies that the concentration of other species affects the synthesis of $\text{SH}\cdot$, which in turn affects the reaction's overall kinetics.

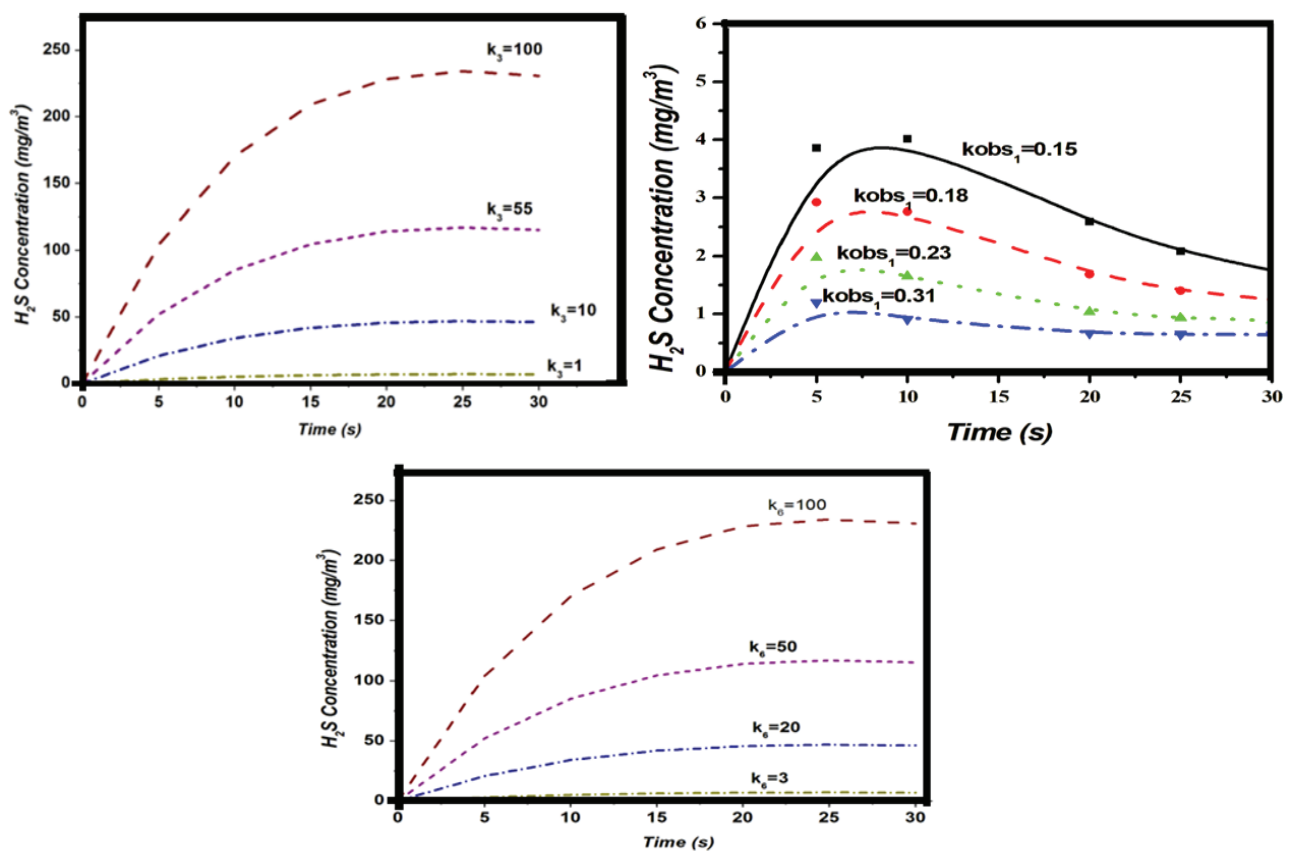


Figure 5. Plot of Influence Concentration profile, versus time t computed with Eq. (14) for different experimental parameter values $k_{\text{obs}1} = 0.15$, $k_{\text{obs}2} = 0.00014$, $k_3 = 0.2 \times 10^2$, $k_6 = 0.2 \times 10^2$.

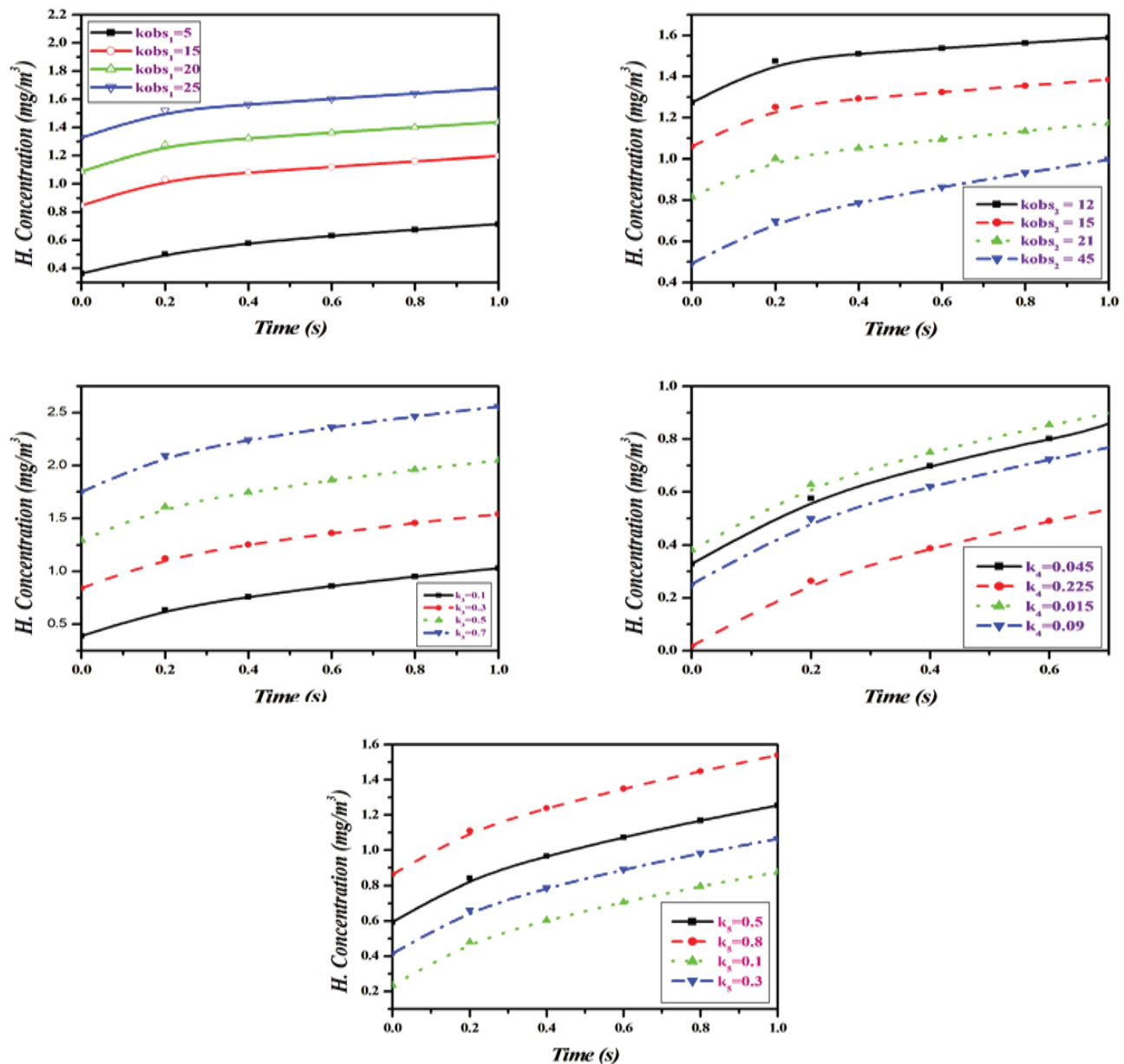


Figure 6. Plot of Influence Concentration profile, versus time t computed with Eq. (15) for different experimental parameter values $k_{\text{obs}1} = 5$, $k_{\text{obs}2} = 12$, $k_3 = 0.1$, $k_4 = 0.045$, $k_5 = 0.5$.

RATE OF DEGRADATION AND MODELED CONCENTRATIONS

The increasing rate of deterioration is depicted in Figure 8, which sheds light on how rapidly H_2S is converted into various products when exposed to UV light. The fluctuating simulated elemental sulfur (S) concentration in Figure 9 suggests that complicated dynamics are at work during the degrading process. The equilibrium between production and consumption in the reaction network may be reflected in the rise and fall of sulfur concentrations.

RESULTS AND DISCUSSION

Major Influence Factors on H_2S Photodegradation

Equations (14-18) denotes the approximate analytical expression for the concentration of H_2S , $\text{H}\cdot$, $\text{SH}\cdot$, H_2 and S. Figure 3 represents the concentration evolution of H_2S , $\text{H}\cdot$, $\text{SH}\cdot$, H_2 and S calculated 2 cm away from the ultraviolet light and showed by the analytical solution (14-18). Figure 4 represents influence concentration for different values (analytical) and compared with experimental results [28]. Figure 5 inferred that the dynamic interaction between the degradation and production of H_2S is depicted by the

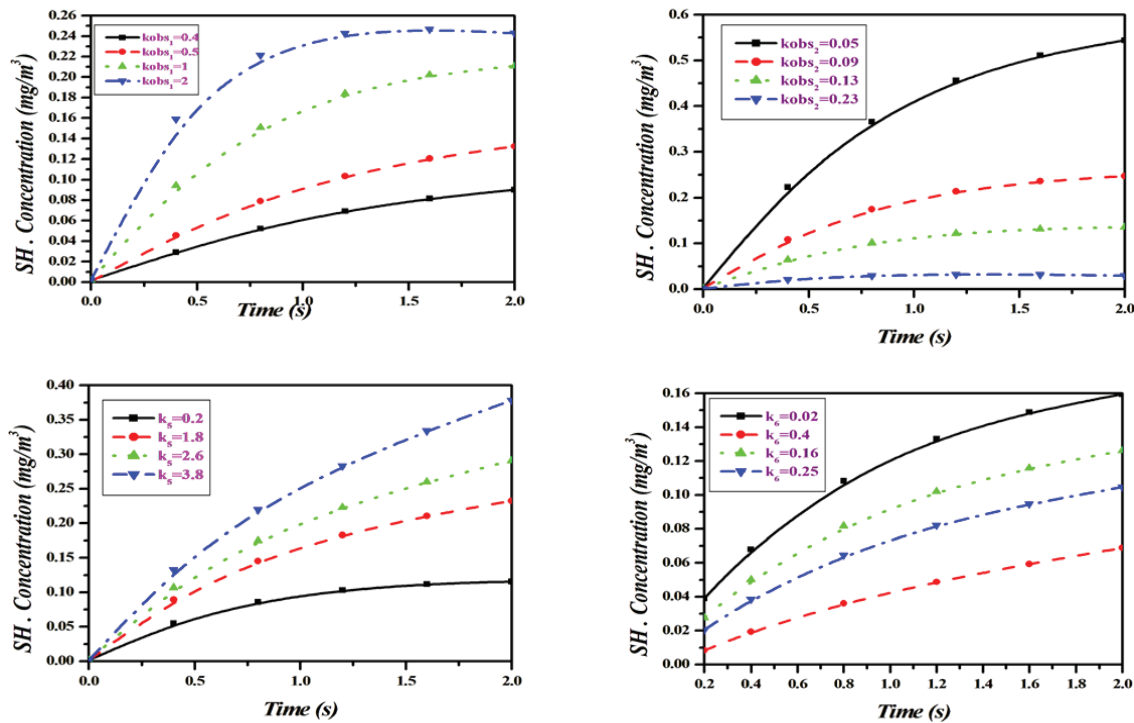


Figure 7. Plot of Influence Concentration profile, versus time t computed with Eq. (16) for different experimental parameter values $k_{\text{obs}1} = 0.4$, $k_{\text{obs}2} = 0.05$, $k_5 = 0.2$, $k_6 = 0.02$.

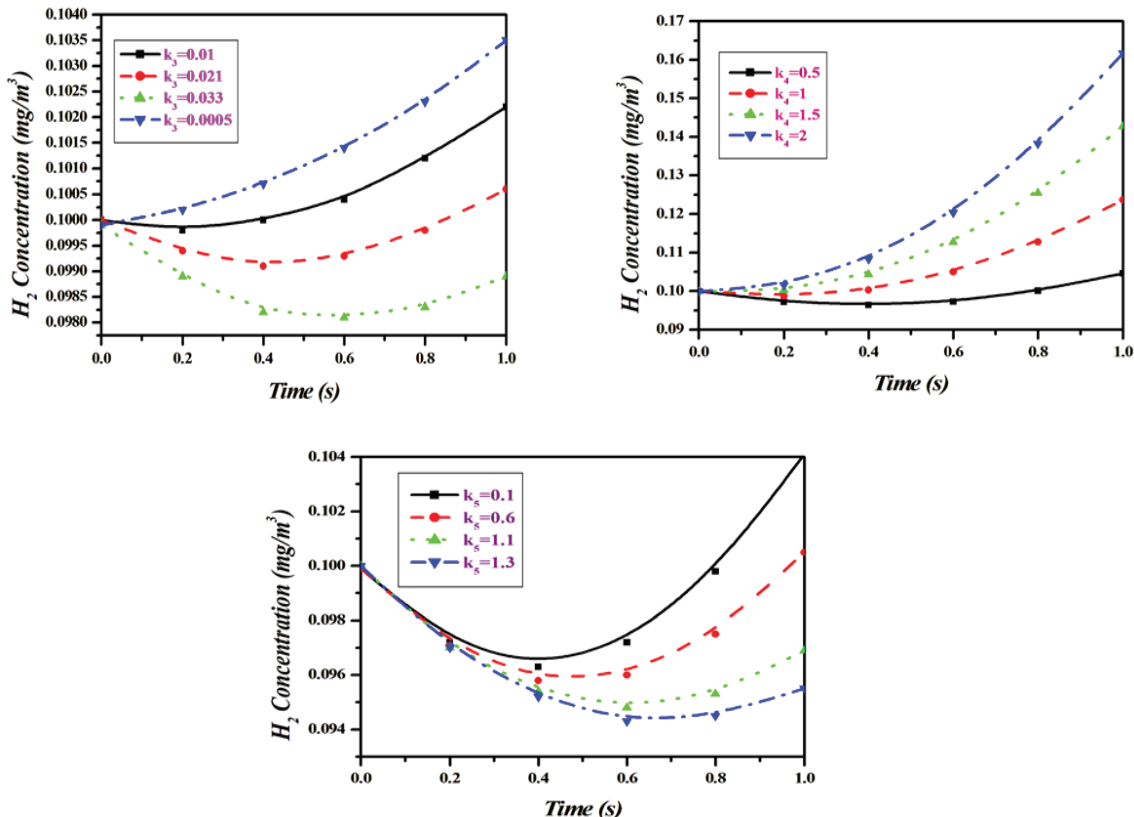


Figure 8. Plot of Influence Concentration profile, versus time t computed with Eq. (17) for different experimental parameter values $k_{\text{obs}1} = 1$, $k_{\text{obs}2} = 0.1$, $k_3 = 0.01$, $k_4 = 0.5$, $k_5 = 0.1$.

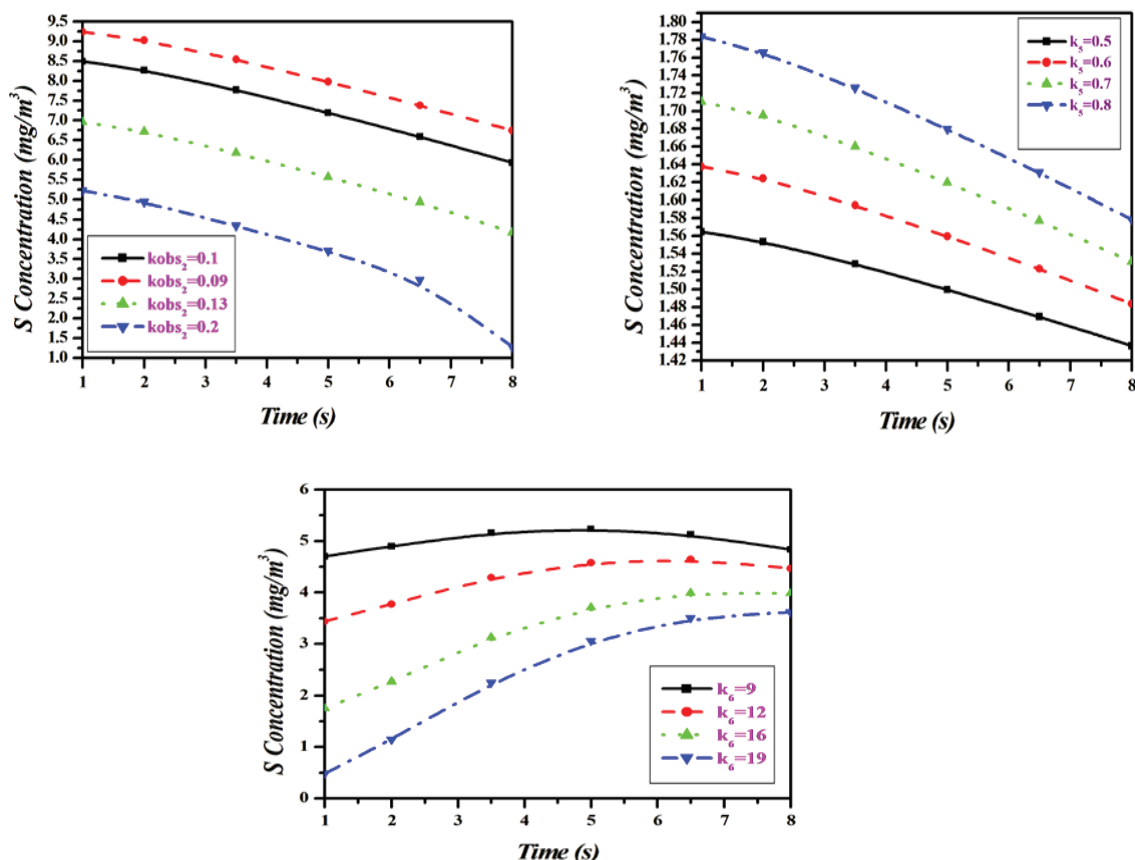


Figure 9. Plot of influence concentration profile, versus time t computed with Eq. (18) for different experimental parameter values $k_{obs1}=1$, $k_{obs2}=0.1$, $k_5=0.5$, $k_6=9$.

rates k_3 , k_6 and the observed degradation constants k_{obs1} , are demonstrated by these graphs. As the generation rate increases, H_2S content tends to accumulate at a faster rate and reach peak concentrations of higher values than normal concentration. From Figure 6, the accumulation of H_2S concentration over time is influenced by the different rate constants (k_{obs1} , k_{obs2} , k_3 , k_4 , k_5) as depicted in the graphs. The accumulation of H_2S is increased and faster with higher values of k_{obs1} , k_{obs2} which represents the observed generation rate. However, it is slower for lower values. In the same way, H_2S buildup is consistently sharpened and increased by concentration profiles when k_3 , k_4 , and k_5 are likely to correspond to these reaction or transport constants. In Figure 7, graphs showing the concentration of SH_2 under different rate constants (k_{obs1} , k_{obs2} , k_5 , k_6) are presented. A graph showing the equilibrium concentrations of SH_2 on the top left-right is shown where k_{obs1} (0.4 to 2) increases. In the same way, the top right-hand side displays a consistent pattern for k_{obs2} across varying values from 0.05 to 0.23, indicating that higher morality values result in greater generation rates. SH_2 buildup is accelerated at values of higher k_5 (0.2–3.8), with the most important effect on the dynamics of generation, as shown in the lower-left section of this diagram. Figure 8 depicts the data emanating from

the three plots and displays the influence of parameters k_3 , k_4 and k_5 on the quantity of H_2S at different times. The top-left plot claims that the increase in k_3 is the reason why the H_2S remains still because in this case, the rate of production could be the factor. In contrast, on the top-right plot, the higher k_4 switch over is the main reason for H_2S getting fast and at a broader level and it is the k_4 which is said to be the real catalyst of the reaction. Figure 9 represents that these plots provide information as to whether k_{obs2} , k_5 and k_6 parameters effect the concentration of S over time. In the top-left plot, the increase in k_{obs2} (0.1 to 0.2) run the S depletion. Consequently, this demonstrates that k_{obs2} is the factor responsible for treatment of the S , which is produced by the reaction being consumed or decaying.

Limitations of The Model

In the suggested model, valuable insights into the UV degradation kinetics of H_2S in the absence of oxygen have been provided. Yet, the model does have several drawbacks, which warrant acknowledgment. The model developed assumes idealistic conditions consisting of unvarying UV light intensity and a homogeneous gas distribution—that may expressly lack realism due to experimental variations such as lamp intensity fluctuations, ambient temperature

Research Focus	Emerging Trends	Key Challenges
Exploration of MOFs	MOFs can be used for gas separation and selective catalysis because of their enormous surface area and adjustable porosity.	The capacity to scale MOF synthesis for industrial use while preserving stability during refining.
Development of Perovskite-based Catalysts	Perovskites are becoming more and more popular because of their capacity to replace noble metals in catalytic reactions and their thermal stability.	Perovskites: incorporation into current technologies and dealing with deactivation over time
Multi-functional Catalysts	In order to increase efficiency and decrease process complexity, multi-functional catalysts have been developed to carry out many reactions concurrently.	Juggling stability, selectivity, and activity in intricate industrial processes.
Catalyst Regeneration and Recycling Techniques	Improved regeneration and recycling techniques are being used to extend the catalyst's lifespan while lowering waste and operating expenses.	Striking a balance between stability, selectivity, and activity in intricate industrial processes.

changes, gas flow turbulence, etc. Hence, any presence of catalyst is not accounted for: catalysts change degradation pathways and significantly affect degradation efficiency. Potential limitations deriving from radical recombination or secondary reactions that would affect intermediate concentrations ($\text{SH}\cdot$, $\text{H}\cdot$) are also disregarded. Uncertainties in reaction rate constants and molar absorptivity values obtained from literature sources add to the sensitivity of the model parameters, which have not been addressed via sensitivity analysis. Since the model assumes perfect mixing and negligible mass transfer resistance, its prediction power may be limited when subjected to scale-up for practical operations.

Sensitivity Analysis

We performed sensitivity analysis on certain key parameters such as rate constants and molar absorptivity to assess the kinetic model's robustness. It inherently implies that the degradation rate is highly sensitive to the variation in the rate constant k with a change of $\pm 10\%$. k causes the predicted concentration profile to vary by up to $\pm 12\%$. The model exhibited somewhat less sensitivity with respect to the variation in the molar absorptivity, which has a direct bearing on the rate of photon absorption and thus the generation of reactive species. Uncertainty in these parameters due to literature variability and measurement limitations was carried out by parametric variation, and the results were then compared with the experimental data. This analysis shows that a few deviations in parameter values may cause variations in how accurately degradation profiles can be predicted, thus emphasizing the need for accurate experimental calibration, although degradation trend capture remains reliable using the model.

Future Directions for Research

Currently, research on catalyst development is moving in a number of encouraging directions with the goal

of resolving present problems and improving petroleum refining systems. Filling some research gaps can have a big impact on how improved catalysts are used in petroleum refining. One important area is lowering the price of innovative materials, like mixed metal oxides and nanocatalysts, which can be costly because of their complicated production procedures and high material costs. Advanced catalysts can become more commercially viable on a wide scale by lowering these expenses.

The integration of multifunctional catalysts and their scalability are two more crucial areas. These catalysts, which are made to carry out several reactions in one step, could streamline refining procedures, lower energy costs, and boost operational effectiveness. But for these multipurpose catalysts, striking a balance between stability, selectivity, and activity can be challenging, particularly when transferring from lab settings to large-scale refinery applications. Improving catalyst stability in the challenging circumstances of industrial refining is still a top concern. Current catalysts, including Co-Mo and Ni-Mo, require expensive regeneration procedures because they can get deactivated by contaminants like sulphur and nitrogen. Creating formulations that are tolerant of sulphur and improving regeneration methods may increase catalyst lifespans and reduce operating expenses. Future studies can offer a road map for the creation of sophisticated refining catalysts that complement the sector's two objectives of boosting sustainability and efficiency by concentrating on these three areas: stability, scalability, and cost reduction.

CONCLUSION

The proposed model of UV degradation of H_2S has been established without the presence of oxygen, and the impact of the primary H_2S concentration and gas preservation duration on the photodegradation experiment was

linked to the analytical results. This study ended by showing how different starting amounts of H_2S and exposure times affected the degradation results, and it compared these real findings with what the model predicted. The mechanisms and reaction kinetics of H_2S degradation in the absence of oxygen are also examined in this study. The findings of this study are expected to significantly improve the sustainability and viability of biogas as a renewable energy source by removing H_2S in anaerobic environments. In this work, the UV deterioration of H_2S without O_2 was represented mathematically. Additionally, it verified the model and investigated how the initial H_2S concentration and gas retention time affected the rate of photodegradation. This study provides both an approximation and a closed analytical representation form of the concentration of H_2S , $\text{H}\cdot$, $\text{SH}\cdot$, H_2 , and S . It also solves the nonlinear differential equations in the VUV degradation analytically using HPM. These special analytical results allow for parameter optimization of VUV photodegradation of H_2S without the presence of oxygen and provide an intuitive understanding of the system.

NOMENCLATURE

H_2S	Influence Concentration (mg/m^3)
$\text{H}\cdot$	Influence Concentration (mg/m^3)
$\text{SH}\cdot$	Influence Concentration (mg/m^3)
H_2	Influence Concentration (mg/m^3)
S	Influence Concentration (mg/m^3)
$k_{\text{obs}1}$	Rate Constants ($\text{m}^{-1}\text{s}^{-1}$)
$k_{\text{obs}2}$	Rate Constants ($\text{m}^{-1}\text{s}^{-1}$)
k_3	Rate Constants ($\text{m}^{-1}\text{s}^{-1}$)
k_4	Rate Constants ($\text{m}^{-1}\text{s}^{-1}$)
k_5	Rate Constants ($\text{m}^{-1}\text{s}^{-1}$)
k_6	Rate Constants ($\text{m}^{-1}\text{s}^{-1}$)

ACKNOWLEDGEMENT

The authors thank King Department of Mathematics, Saveetha School of Engineering, SIMATS, Chennai, Tamil Nadu, and India for the support and facilities that made this research possible.

AUTHORSHIP CONTRIBUTIONS

V. Sreelatha Devi & K. Saranya : Writing- Original draft preparation, Investigation and Editing. Vijayabalan D : Conceptualization, Visualization. Muthumari G: Methodology, Editing. K A. Niranjan kumar& Banu Priya V: Supervision, Validation, and Reviewing

DATA AVAILABILITY STATEMENT

The authors confirm that the data that supports the findings of this study are available within the article. Raw data that support the finding of this study are available from the corresponding author, upon reasonable request

CONFLICT OF INTEREST

The author declared no potential conflicts of interest with respect to the research, authorship, and/or publication of this article.

ETHICS

There are no ethical issues with the publication of this manuscript. Funding the authors confirm there is no source of funding for this research.

REFERENCES

- [1] Occupational Safety and Health Administration. Hydrogen Sulfide Hazards. Available at: <https://www.osha.gov/hydrogen-sulfide/hazards>. Accessed on May 7, 2021.
- [2] Beauchamp RO, Bus JS, Popp JS, Boreiko CJ, Andjelkovich DA, Leber P, et al. A critical review of the literature on hydrogen sulfide toxicity. *Crit Rev Toxicol* 1984;13:25–97. [\[CrossRef\]](#)
- [3] Reiffenstein RJ, Hulbert WC, Roth SH. Toxicology of hydrogen sulfide. *Annu Rev Pharmacol Toxicol* 1992;32:109–134. [\[CrossRef\]](#)
- [4] Mokhatab S, Poe WA, Mak JY. Basic Concepts of Natural Gas Processing. In: *Handbook of Natural Gas Transmission and Processing*. 4th ed. Gulf Professional Publishing; 2019. p. 177–189. [\[CrossRef\]](#)
- [5] Mohtadi R, Lee WK, Cowan S, Van Zee JW, Murthy M. Effects of hydrogen sulfide on the performance of a PEMFC. *Electrochem Solid-State Lett* 2003;6:A272. [\[CrossRef\]](#)
- [6] Du Z, Liu C, Jhai J, Guo X, Xiong Y, Su W, et al. A review of hydrogen purification technologies for fuel cell vehicles. *Catalysts* 2021;11:393. [\[CrossRef\]](#)
- [7] Hassan TNAT, Shariff AM, Pauzi MMM, Khidzir MS, Surmi A. Insights on cryogenic distillation technology for simultaneous CO_2 and H_2S removal for sour gas fields. *Molecules* 2022;27:1424. [\[CrossRef\]](#)
- [8] Northrop PS, Valencia JA. The CFZ TM process: A cryogenic method for handling high- CO_2 and H_2S gas reserves and facilitating geosequestration of CO_2 and acid gases. *Energy Procedia* 2009;1:171–177. [\[CrossRef\]](#)
- [9] Hashemi SE, Sarker S, Lien KM, Schnell SK, Austbø B. Cryogenic vs. absorption biogas upgrading in liquefied biomethane production – An energy efficiency analysis. *Fuel* 2019;245:294–304. [\[CrossRef\]](#)
- [10] Rex P, Meenakshisundaram N, Barmavatu P. Sustainable valorisation of kitchen waste through greenhouse solar drying and microwave pyrolysis technology readiness level for the production of biochar. *J Environ Health Sci Eng* 2024;22:381–395. [\[CrossRef\]](#)

[11] Mariyappillai V, Shiyamala C, Abishek T, Tiffany M, Pandiyan V, Senthilraja A, et al. Zr-modified ZnO nanoparticles: Optimized photocatalytic degradation and antibacterial efficiency for pollution control. *Ceram Int* 2025. doi: 10.1016/j.ceramint.2025.02.402. [\[CrossRef\]](#)

[12] Leela NS, Kannan S, Abishek T, Tiffany M, Pandiyan V, Periyasami G, et al. Enhanced photocatalytic activity of azo dyes degradation by urea assisted Mo-doped TiO₂ under UV-A light and sun-light irradiation. *J Alloys Compd* 2025;1020:179389. [\[CrossRef\]](#)

[13] Alshoaibi A, Ramgopal NC, Ramasundaram S, Upendranath K, Mahanthappa M, Fahad M, et al. NiS/NiS₂-embedded sulfur-doped porous graphitic carbon nitride nanosheets as an efficient catalyst for 4-Nitrophenol reduction. *Diamond Relat Mater* 2025;153:112110. [\[CrossRef\]](#)

[14] Mahmoud AS, Abubakar MH, Adamu Z. Demolition wastes in the global construction industry: An overview of research perspective from 2001 to 2020. *J Therm Eng* 2025;11(2):603–621. [\[CrossRef\]](#)

[15] Pathak B, Patel N. Effect of modifying bowl geometry for IC engine fueled with diesel and biofuel: Review. *J Therm Eng* 2024;10(1):244–261. [\[CrossRef\]](#)

[16] Pudi A, Rezaei M, Signorini V, Andersson MP, Baschetti MG, Mansouri SS. Hydrogen sulfide capture and removal technologies: A comprehensive review of recent developments and emerging trends. *Sep Purif Technol* 2022;298:121448. [\[CrossRef\]](#)

[17] Silvestre G, Fernandez B, Bonmati A. Significance of anaerobic digestion as a source of clean energy in waste water treatment plants. *Energy Convers Manag* 2015;101:255–262. [\[CrossRef\]](#)

[18] Montebello AM, Mora M, López LR, Bezerra T, Gamisans X, Lafuente J, et al. Aerobic desulfurization of biogas by acidic biotrickling filtration in a randomly packed reactor. *J Hazard Mater* 2014;280:200–208. [\[CrossRef\]](#)

[19] Song X, Yao W, Zhang B, Wu Y. Application of Pt/CdS for the photocatalytic flue gas desulfurization. *Int J Photoenergy* 2012;2012:684735. [\[CrossRef\]](#)

[20] Guldal NO, Figen HE, Baykara SZ. New catalysts for hydrogen production from H₂S: Preliminary results. *Int J Hydrog Energy* 2015;40(24):7452–7458. [\[CrossRef\]](#)

[21] Akamatsu K, Nakane M, Sugawara T, Hattori T, Nakao S. Development of a membrane reactor for decomposing hydrogen sulfide into hydrogen using a high performance amorphous silica membrane. *J Membr Sci* 2008;325(1):16–19. [\[CrossRef\]](#)

[22] Anani AA, Mao Z, White RE, Srinivasan S, Appleby AJ. Electrochemical production of hydrogen and sulfur by low-temperature decomposition of hydrogen sulfide in an aqueous alkaline solution. *J Electrochem Soc* 1990;137(9):2703–2709. [\[CrossRef\]](#)

[23] Zong X, Han J, Seger B, Chen H, Lu G, Li C, et al. An integrated photo electrochemical chemical loop for solar-driven overall splitting of hydrogen sulfide. *Angew Chem* 2014;53(17):4399–4403. [\[CrossRef\]](#)

[24] Bai X, Cao Y, Wu W. Photocatalytic decomposition of H₂S to produce H₂ over CdS nanoparticles formed in HY-zeolite pore. *Renew Energy* 2011;36(10):2589–2592. [\[CrossRef\]](#)

[25] Yan H, Yang J, Ma G, Wu G, Zong X, Lei Z, et al. Visible-light-driven hydrogen production with extremely high quantum efficiency on Pt-PdS/CdS photocatalyst. *J Catal* 2009;266(2):165–168. [\[CrossRef\]](#)

[26] Reddy EL, Karuppiah J, Biju VM, Subrahmanyam C. Catalytic packed bed non-thermal plasma reactor for the extraction of hydrogen from hydrogen sulfide. *Int J Energy Res* 2013;37(11):1280–1286. [\[CrossRef\]](#)

[27] John S, Hamann JC, Muknahallipatna SS, Legowski S, Ackerman JF, Argyle MD. Energy efficiency of hydrogen sulfide decomposition in a pulsed corona discharge reactor. *Chem Eng Sci* 2009;64(23):4826–4834. [\[CrossRef\]](#)

[28] Xu JH, Ding BB, Lv XM, Lan SH, Li CL, Pen L. Mathematical modeling and mechanism of VUV photodegradation of H₂S in the absence of O₂. *Int J Photoenergy* 2018;2018:2769213. [\[CrossRef\]](#)

[29] Xu MY, Zeng C, Lin YL, Zhang TY, Fu Q, Zhao HX, et al. Wavelength dependency and photosensitizer effects in UV-LED photodegradation of iohexol. *Water Res* 2024;255:121477. [\[CrossRef\]](#)

[30] Liu J, Zhang J, Jia M, Ma R, Qu R, Wang Z, et al. Efficient photocatalytic degradation of imidazolium ionic liquids in an N-ZnO/simulated sunlight irradiation system and its mechanism. *Chem Eng J* 2024;154317. [\[CrossRef\]](#)

[31] Wilson SHS, Howe JD, Ashfold MNR. On the near ultraviolet photodissociation of hydrogen sulphide. *Mol Phys* 1996;88(3):841–858. [\[CrossRef\]](#)

[32] Sokhansanj A, Haghghi M, Shabani M. Developing the novel model for kinetics and mass transfer in sun light driven photodegradation of malachite green over Bi₂O₂CO₃/CuBi₂O₄ (50: 50) flower-like nanophotocatalyst: Machine and deep-learning algorithms. *Process Saf Environ Prot* 2024;184:502–522. [\[CrossRef\]](#)

[33] Wang Y, Xu D, Yang X, He JH. Novel 2D/2D S-scheme heterojunction photocatalyst for peroxymonosulfate activation enables ciprofloxacin ultrafast degradation: High-efficiency photogenerated carrier transport. *Chem Eng J* 2024;488:150844. [\[CrossRef\]](#)

[34] He JH. Homotopy perturbation technique. *Comput Methods Appl Mech Eng* 1999;178:257–262. [\[CrossRef\]](#)

[35] He JH. A coupling method of homotopy technique and a perturbation technique for non-linear problems. *Comput Methods Appl Mech Eng* 2000;35:37–43. [\[CrossRef\]](#)

[36] Saranya K, Iswarya T, Mohan V, Sathappan KE, Rajendran L. Mathematical modeling of glucose, insulin, b-cell mass: Homotopy perturbation method approach. *Eur J Mol Clin Med* 2020;07(02):3513–3530.

[37] Saranya K, Mohan V, Kizek R, Fernandez C, Rajendran L. Unprecedented homotopy perturbation method for solving nonlinear equations in the enzymatic reaction of glucose in a spherical matrix. *Bioprocess Biosyst Eng* 2017;41:281–294. [\[CrossRef\]](#)

[38] He JH. Homotopy perturbation method: A new nonlinear analytical technique. *Appl Math Comput* 2003;135:73–79. [\[CrossRef\]](#)

[39] He JH. Homotopy perturbation method for solving boundary value problem. *Phys Lett A* 2006;350:87–88. [\[CrossRef\]](#)

[40] He JH. Some asymptotic methods for strongly nonlinear equations. *Int J Mod Phys B* 2006;20:1141–1199. [\[CrossRef\]](#)

[41] Kalachev LV, Seidman TI. Singular perturbation analysis of a stationary diffusion reaction system exhibiting a corner-type behavior in the interval interior. *J Math Anal Appl* 2003;288(2):722–743. [\[CrossRef\]](#)

[42] Khan H, Rajpar AH, Alzabut J, Aslam M, Etemad S, Rezapour S. On a fractal–fractional-based modeling for influenza and its analytical results. *Qual Theory Dyn Syst* 2024;23:7. [\[CrossRef\]](#)

[43] Ahmed S, Azar AT, Abdel-Aty M, Khan H, Alzabut J. A nonlinear system of hybrid fractional differential equations with application to fixed time sliding mode control for leukemia therapy. *Ain Shams Eng J* 2024;102566. [\[CrossRef\]](#)

[44] Khan H, Alzabut J, Gómez-Aguilar JF, Alkhazan A. Essential criteria for existence of solution of a modified-ABC fractional order smoking model. *Ain Shams Eng J* 2024;102646. [\[CrossRef\]](#)

[45] Enokihara GH, Loures CCA, Izálio Filho HJ, Alcântara MAK, Siqueira AF, Da Rós PCM, et al. Kinetic modelling of total organic carbon degradation in dairy wastewater. *Environ Technol* 2024;45(5):880–887. [\[CrossRef\]](#)

[46] Liu T, Ding Z, Yu J, Zhang W. Parameter estimation for nonlinear diffusion problems by the constrained homotopy method. *Mathematics* 2023;11(12):2642. [\[CrossRef\]](#)

[47] Liu T, Xue R, Liu C, Qi Y. A regularization homotopy strategy for the constrained parameter inversion of partial differential equations. *Entropy* 2021;23(11):1480. [\[CrossRef\]](#)

[48] Sander SP, Abbatt J, Barker JR, et al. Chemical Kinetics and Photochemical Data for Use in Atmospheric Studies. JPL Publication; 2011.

[49] Bradley JN, Trueman SP, Whytock DA, Zaleski TA. Electron spin resonance study of the reaction of hydrogen atoms with hydrogen sulphide. *J Chem Soc Faraday Trans 1* 1973;69:416–425. [\[CrossRef\]](#)

[50] Peng J, Hu X, Marshall P. Experimental and ab initio investigations of the kinetics of the reaction of H atoms with H₂S. *J Phys Chem A* 1999;103(27):5307–5311. [\[CrossRef\]](#)

[51] Loraine G, Glaze W. Destruction of vapor phase halogenated methanes by means of ultraviolet photolysis. *Proc Ind Waste Conf* 1993;47:309–316.

[52] Stachnik RA, Molina MJ. Kinetics of the reactions of mercapto radicals with nitrogen dioxide and oxygen. *J Phys Chem* 1987;91(17):4603–4606. [\[CrossRef\]](#)

APPENDIX

Kinetics of UV degradation of hydrogen sulfide without oxidization by Homotopy Perturbation Method

V. Sreelatha DEVI^{1*}, K. SARANYA¹, D. VIJAYABALAN², K A. Niranjan KUMAR³, Muthumari G³, Banu Priya V

Appendix A: Basic Concepts of the HPM

Having successfully overcome many of the limitations of traditional perturbation methods, the HPM has received the attention of many researches in recent decades. The simple implementation of the HPM even when applied to strong nonlinear differential equation is another desired feature that made it one of the most used techniques in recent years. Here, we present a brief introduction to the HPM. Consider the following nonlinear differential equation:

$$L(u) + N(u) - f(r) = 0, r \in \Omega \quad (A1)$$

With boundary conditions

$$B\left(u, \frac{du}{dr}\right) = 0, r \in \Gamma \quad (A2)$$

where L is a linear operator, N is a nonlinear operator, and $f(r)$ is a known analytic function. By the homotopy technique, we construct a homotopy $v(r, p) : \Omega \times [0, 1] \rightarrow R$ that satisfies:

$$H(v, p) = (1-p)(L(v) - L(u_0)) + p(L(v) + N(v) - f(r)) = 0, \quad (A3)$$

where $p \in [0, 1]$ is an embedding parameter, and u_0 is an initial approximation of Eq.(A1) that satisfies the boundary conditions (A2). when $p = 0$, Eq.(A3) become the linear equation

$$L(v) - L(u_0) = 0, \quad (A4)$$

and when $p = 1$, it becomes the nonlinear equation

$$L(u) + N(u) - f(r) = 0, \quad (A5)$$

The process of changing p from zero to unity is the process that changes $v(r, p)$ from $u_0(r)$ to $u(r)$. We first use the embedding parameter p as a “small parameter” and assume that the solution of Eq.(A1) can be written as a power series in p :

$$p^0 : L(v_0) = 0$$

$$p^1 : L(v_1) + N(v_0) - f(r) = 0$$

Solving the above system of equations we obtain v_0, v_1, \dots

$$v = v_0 + p v_1 + p^2 v_2 + \dots \quad (A6)$$

Setting $p = 1$ results in the approximate solution of Eq.(A1):

$$u = \lim_{p \rightarrow 1} v = v_0 + v_1 + v_2 + \dots \quad (A7)$$

Appendix B: Analytical expressions for the concentrations of H_2S , $H.$, $SH.$, H_2 and S are derived from these equations using homotopy perturbation method.

Equation(7-11) using HPM Method

$$\frac{d[H_2S]}{dt} = -k_{obs1}[H_2S] - k_3[H_2S][H.] + k_6[SH.] \quad (B1)$$

$$\frac{d[H.]}{dt} = k_{obs1}[H_2S] + k_{obs2}[SH.] - k_3[H_2S][H.] + k_4[H.]^2 - k_5[SH.][H.] \quad (B2)$$

$$\frac{d[SH.]}{dt} = k_{obs1}[H_2S] + k_{obs2}[SH.] - k_5[SH.][H.] - k_6[SH.]^2 \quad (B3)$$

$$\frac{d[H_2]}{dt} = k_3[H_2S][H.] + k_4[H.]^2 + k_5[H.][SH.] \quad (B4)$$

$$\frac{d[S]}{dt} = k_{obs2}[SH.] - k_5[SH.][H.] - k_6[SH.]^2 \quad (B5)$$

$$u = H_2S, v = H., w = SH., x = H_2S, y = S, k_{obs1} = a, k_{obs2} = b \quad (B6)$$

Substituting all the above values in (B1)-(B5) in (B6)

$$\frac{du}{dt} = -au - k_3uv + k_6w^2 \quad (B7)$$

$$\frac{dv}{dt} = au + bw - k_3uv - k_4v^2 - k_5uv \quad (B8)$$

$$\frac{dw}{dt} = au - bw - k_5vw - k_6w^2 \quad (B9)$$

$$\frac{dx}{dt} = k_3uv + k_4v^2 + k_5uv \quad (B10)$$

$$\frac{dy}{dt} = bw + k_5vw + k_6w^2 \quad (B11)$$

We construct the new homotopy for the equation(7-11) as follows(Rajendran and Anitha(2013))

$$(1-p)\left[\frac{du}{dt} + au\right] + p\left[\frac{du}{dt} + au + k_3uv - k_6w\right] = 0 \quad (B12)$$

$$(1-p)\left[\frac{dv}{dt} - au - bw\right] + p\left[\frac{dv}{dt} - au - bw + k_3uv - k_4v^2 + k_5vw\right] = 0 \quad (B13)$$

$$(1-p) \left[\frac{dw}{dt} - au - bw \right] + p \left[\frac{dw}{dt} - au - bw + k_5vw + k_6w^2 \right] = 0 \quad (B14)$$

$$(1-p) \left[\frac{dx}{dt} \right] + p \left[\frac{dx}{dt} - k_3uv - k_4v^2 + k_5vw \right] = 0 \quad (B15)$$

$$(1-p) \left[\frac{dy}{dt} - bw \right] + p \left[\frac{dy}{dt} - bw + k_5vw + k_6v^2 \right] = 0 \quad (B16)$$

When $p \in (0,1)$ is an embedding parameter, Now assume that the solution of the equation (7-11) are

$$u = u_0 p^0 + u_1 p^1 + u_2 p^2 + u_3 p^3 + \dots \quad (B17)$$

$$v = v_0 p^0 + v_1 p^1 + v_2 p^2 + v_3 p^3 + \dots \quad (B18)$$

$$w = w_0 p^0 + w_1 p^1 + w_2 p^2 + w_3 p^3 + \dots \quad (B19)$$

$$x = x_0 p^0 + x_1 p^1 + x_2 p^2 + x_3 p^3 + \dots \quad (B20)$$

$$y = y_0 p^0 + y_1 p^1 + y_2 p^2 + y_3 p^3 + \dots \quad (B21)$$

Substituting the above equation (B1 - B5) and equating the coefficients p^0, p^1, \dots on both sides we get, Using HPM,

$$p^0 = \frac{du_0}{dt} + au_0 = 0 \quad (B22)$$

$$p^1 = \frac{du_1}{dt} + au_1 + k_3u_0v_0 - k_6w_0^2 = 0 \quad (B23)$$

$$p^0 = \frac{dv_0}{dt} - au_0 - bw_0 = 0 \quad (B24)$$

$$p^1 = \frac{dv_1}{dt} - au_1 - bw_1 + k_3u_0v_0 - k_4v_0^2 + k_5v_0w_0 = 0 \quad (B25)$$

$$p^0 = \frac{dw_0}{dt} - au_0 + bw_0 = 0 \quad (B26)$$

$$p^1 = \frac{dw_1}{dt} - au_1 + bw_1 + k_5v_0w_0 + k_6w_0^2 = 0 \quad (B27)$$

$$p^0 = \frac{dx_0}{dt} = 0 \quad (B28)$$

$$p^1 = \frac{dx_1}{dt} - k_3u_0v_0 - k_4v_0^2 - k_5v_0w_0 = 0 \quad (B29)$$

$$p^0 = \frac{dy_0}{dt} - bw_0 = 0 \quad (B30)$$

$$p^1 = \frac{dy_1}{dt} - bw_1 - k_5v_0w_0 - k_6w_0^2 = 0 \quad (B31)$$

Solving the initial and boundary condition are in

where

$$k_{obs1} = a; k_{obs2} = b; c_1 = u_{ini}; A = \frac{au_{ini}}{a-b}; B = w_{ini} - \frac{au_{ini}}{a-b};$$

$$c_2 = v_{ini} + \left[\frac{au_{ini} + bA}{a} \right] + 1;$$

$$c_3 = \frac{au_{ini} + bA}{a}; c_4 = ab(a-b); c_5 = 2A^2ABk_6; c_6 = 2A^2ABk_6; c_7 = a^2bc_1c_2k_3;$$

$$c_8 = a^2c_1k_3; c_9 = -a^2c_1k_3; c_{10} = 2A^2b^2k_6; c_{11} = aA^2bk_6; c_{12} = aA^2bk_6;$$

$$c_{13} = 4aAbBk_6; c_{14} = 4aAbBk_6; c_{15} = 2ab^2c_1c_2k_3; c_{16} = 2b^2c_1c_3k_3;$$

$$\begin{aligned}
c_{17} &= 2b^2c_1c_3k_3; \quad c_{18} = abB^2k_6; \quad c_{19} = abc_1c_3k_3; \quad c_{20} = abc_1c_3k_3; \\
c_{21} &= 2abc_1k_3; \quad c_{22} = 2abc_1k_3; \quad c_{23} = 2A^2B^2k_6; \quad c_{24} = 2b^2c_1c_3k_3; \\
L_1 &= c_5 + c_8 - c_{10} + c_{12} - c_{14} - c_{16} - c_{17} + c_{20} - c_{22} \\
L_2 &= -c_6 + c_9 + c_{21} + c_{13}L_3 = -c_{11} - c_{19} + c_{23} + c_{24}L_4 = c_{15} - c_{17} \\
p_1 &= -2c_{18}a^5; \quad p_2 = 2c_{18}a^5; \quad p_3 = 5bc_{18}a^4; \quad p_4 = 5bc_{18}a^4; \\
p_5 &= 2Bc_4k_5a^4; \quad p_6 = 2Bc_4k_5a^4; \quad p_7 = 2B^2c_4k_6a^4; \quad p_8 = 2B^2c_4k_6a^4; \quad p_9 = 2bL_1a^4; \\
p_{10} &= 2bL_1a^4; \quad p_{11} = 2bL_2a^4; \quad p_{12} = 2bL_2a^4; \quad p_{13} = bL_3a^4; \quad p_{14} = bL_3a^4; \\
p_{15} &= 2bBc_2c_4k_5ta^4; \quad p_{16} = 2bL_4a^4; \quad p_{17} = 4b^2c_{18}a^3; \quad p_{18} = 4b^2c_{18}a^3; \\
p_{19} &= 5bBc_4k_5a^3; \quad p_{20} = Abc_3c_4k_5a^3; \quad p_{21} = 2Abc_4k_5a^3; \quad p_{22} = 2bBc_3c_4k_5a^3; \\
p_{23} &= 2Abc_4k_5a^3; \quad p_{24} = 5bBc_4k_5a^3; \quad p_{25} = 2Abc_2c_4k_5a^3; \quad p_{26} = Abc_3c_4k_5a^3; \\
p_{27} &= 2bBc_3c_4k_5a^3; \quad p_{28} = 2Abc_2c_4k_5a^3; \quad p_{29} = 5bB^2c_4k_6a^3; \quad p_{30} = A^2bc_4k_6a^3; \\
p_{31} &= 4AbBc_4k_6a^3; \quad p_{32} = 5bB^2c_4k_6a^3; \quad p_{33} = A^2bc_4k_6a^3; \quad p_{34} = 4AbBc_4k_6a^3; \\
p_{35} &= 3b^2L_1a^3; \quad p_{36} = 3b^2L_1a^3; \quad p_{37} = 5b^2L_2a^3; \quad p_{38} = 5b^2L_2a^3; \\
p_{39} &= 2b^2L_3a^3; \quad p_{40} = 2b^2L_3a^3; \quad p_{41} = 2bL_4a^3; \quad p_{42} = 2bL_4a^3; \\
p_{43} &= 5b^2Bc_2c_4k_5a^3; \quad p_{44} = 3b^2L_4a^3; \quad p_{45} = b^3c^{18}a^2; \quad p_{46} = b^3c^{18}a^2; \\
p_{47} &= 4b^2Bc_4k_5a^2; \quad p_{48} = 2Ab^2c_3c_4k_5a^2; \quad p_{49} = 5Ab^2c_4k_5a^2; \quad p_{50} = 5b^2Bc_3c_4k_5a^2; \\
p_{51} &= 5Ab^2c_4k_5a^2; \quad p_{52} = 4b^2Bc_4k_5a^2; \quad p_{53} = 3Ab^2c_2c_4k_5a^2; \quad p_{54} = 2Ab^2c_3c_4k_5a^2; \\
p_{55} &= 2Ab^2c_3c_4k_5a^2; \quad p_{56} = 5b^2Bc_3c_4k_5a^2; \quad p_{57} = 3Ab^2c_2c_4k_5a^2; \quad p_{58} = 4b^2B^2c_4k_6a^2; \\
p_{59} &= 2A^2b^2c_4k_6a^2; \quad p_{60} = 10Ab^2Bc_4k_6a^2; \quad p_{61} = 2A^2b^2Bc_4k_6a^2; \quad p_{62} = 4b^2B^2c_4k_6a^2; \\
p_{63} &= 10Ab^2Bc_4k_6a^2; \quad p_{64} = b^3L_1a^2; \quad p_{65} = b^3L_2a^2; \quad p_{66} = 4b^3L_2a^2; \\
p_{67} &= b^3L_3a^2; \quad p_{68} = b^3L_3a^2; \quad p_{69} = b^2L_4a^2; \quad p_{70} = b^2L_4a^2; \\
p_{71} &= 4b^3Bc_2c_4k_5a^2; \quad p_{72} = b^3L_4a^2; \quad p_{73} = b^3Bc_4k_5a; \quad p_{74} = Ab^3c_3c_4k_5a; \\
p_{75} &= 4Ab^3Bc_4k_5a; \quad p_{76} = 4b^3Bc_3c_4k_5a; \quad p_{77} = 4Ab^3c_4k_5a; \quad p_{78} = b^3Bc_4k_5a; \\
p_{79} &= Ab^3c_2c_4k_5a; \quad p_{80} = Ab^3c_3c_4k_5a; \quad p_{81} = 4b^3Bc_3c_4k_5a; \quad p_{82} = Ab^3c_2c_4k_5a; \\
p_{83} &= b^3B^2c_4k_6a; \quad p_{84} = A^2b^3c_4k_6a; \quad p_{85} = 8Ab^3c_4k_6a; \quad p_{86} = A^2b^3c_4k_6a; \\
p_{87} &= 8Ab^3c_4k_6a; \quad p_{88} = 8Ab^3c_4k_6a; \quad p_{89} = b^4L_2a; \quad p_{90} = b^4L_2a; \\
p_{91} &= b^4Bc_2c_4k_5a; \quad p_{92} = Ab^4c_4k_5; \quad p_{93} = b^4Bc_3c_4k_5; \quad p_{94} = Ab^4c_4k_5; \\
p_{95} &= b^4Bc_3c_4k_5; \quad p_{96} = 2Ab^4Bc_4k_6; \quad p_{97} = 2Ab^4Bc_4k_6; \quad p_{98} = a(a-b)^2(2a-b)bc_4; \\
A_1 &= p_1 + p_3 - p_5 + p_7 - p_{17} + p_{19} - p_{29} + p_{45} - p_{47} + p_{57} + p_{73} - p_{83} \\
A_2 &= p_2 - p_4 + p_6 - p_8 + p_9 - p_{12} + p_{14} - p_{15} + p_{18} + p_{23} - p_{24} - p_{25} + p_{26} + p_{27} + p_{32} \\
&\quad - p_{33} - p_{34} - p_{35} + p_{38} - p_{40} - p_{41} - p_{46} + p_{49} - p_{51} + p_{52} + p_{53} - p_{54} \\
&\quad - p_{55} + p_{60} - p_{61} + p_{62} + p_{63} - p_{66} + p_{68} + p_{69} + p_{77} - p_{78} - p_{79} + p_{80} \\
&\quad + p_{81} - p_{86} + p_{87} + p_{90} + p_{88} - p_{94} - p_{95} + p_{97}; \\
A_3 &= p_{11} - p_{37} + p_{65} - p_{89}; \\
A_4 &= -p_{10} + p_{28} + p_{36} + p_{42} - p_{56} - p_{64} - p_{70} + p_{82}; \\
A_5 &= -p_{13} - p_{20} + p_{30} + p_{39} - p_{58} - p_{67} - p_{74} + p_{84} + p_{48}; \\
A_6 &= -p_{21} - p_{22} + p_{31} + p_{50} - p_{59} + p_{85} + p_{92} + p_{93} - p_{96} - p_{75} - p_{76}; \\
\end{aligned}$$

Applying boundary Conditions, substituting and simplifying all the values, then

$$\begin{aligned}
u(t) &= \frac{1}{c_4} \left[e^{-at} \left[L_1 - L_4 t \right] - e^{-at-bt} L_2 + L_3 e^{-2at} + c_{18} e^{-2bt} \right] \\
v(t) &= \frac{a}{c_4} \left[\left[e^{-at} \left[L_4 \right] + \left[L_1 - L_4 t \right] \left[e^{-at} \right] \left[-a \right] + e^{-at-bt} (a+b)L_2 + L_3 e^{-2at} (-2a) + c_{18} e^{-2bt} (-2b) \right] e^{-at} L_1 - L_4 \left[t e^{-at} \right] \right]
\end{aligned}$$

$$w(t) = \frac{e^{-at-bt-(2a+b)t}}{p_{98}} \left[\begin{array}{l} \left[e^{3at} (A_1) + e^{at+(2a+b)t} (A_2 + p_{43}t - p_{71}t + p_{91}t) \right] \\ \left[+ e^{(2a+b)t} (A_3) + e^{at+(b-a)t+(2a+b)} (A_4 + p_{16}t - p_{44}t + p_{72}t) \right] \\ \left[+ e^{at+2bt} (A_5) + e^{at+(a+b)} (A_6) \right] \end{array} \right]$$

$$X_1(t) = -k_3 c_1 c_3 \frac{-2at}{-2a} - k_3 c_1 \frac{-(a+b)t}{-(a+b)} - c_1 c_2 k_3 \frac{-at}{-a} +$$

$$k_4 \left[c_3^2 \frac{-2at}{-2a} + 2c_3 \frac{-(a+b)t}{-(a+b)} - 2c_3 c_2 \frac{-at}{-a} - 2c_2 \frac{-bt}{-b} + \frac{e^{-2bt}}{-2b} + c_2^2 t \right] +$$

$$k_5 \left[-A \frac{-(a+b)t}{-(a+b)} - A c_3 \frac{-2at}{-2a} + A c_2 \frac{-at}{-a} - B c_3 \frac{-(a+b)t}{-(a+b)} + B c_2 \frac{-bt}{-b} - B \frac{e^{-2bt}}{-2b} \right]$$